MOX-Report No. 80/2020

Hemodynamics of the heart's left atrium based on a Variational Multiscale-LES numerical model

Zingaro, A.; Dede', L.; Menghini, F.; Quarteroni, A.

MOX, Dipartimento di Matematica
Politecnico di Milano, Via Bonardi 9 - 20133 Milano (Italy)

mox-dmat@polimi.it http://mox.polimi.it

Hemodynamics of the heart's left atrium based on a Variational Multiscale-LES numerical model

Alberto Zingaro[a,*], Luca Dede'[a], Filippo Menghini[b], Alfio Quarteroni[a,c]

[a] *MOX, Dipartimento di Matematica, Politecnico di Milano, Piazza Leonardo da Vinci 32, 20133, Milan, Italy*

[b] *Casale SA, Via Giulio Pocobelli 6, CH-6900 Lugano, Switzerland*

[c] *Chair of Modelling and Scientific Computing (CMCS), Institute of Mathematics, École Polytechnique Fédérale de Lausanne, Station 8, Av. Piccard, CH-1015 Lausanne, Switzerland*

Abstract

In this paper, we investigate the hemodynamics of a left atrium (LA) by proposing a computational model suitable to provide physically meaningful fluid dynamics indications and detailed blood flow characterization. In particular, we consider the incompressible Navier-Stokes equations in Arbitrary Lagrangian Eulerian (ALE) formulation to deal with the LA domain under prescribed motion. A Variational Multiscale (VMS) model is adopted to obtain a stable formulation of the Navier-Stokes equations discretized by means of the Finite Element method and to account for turbulence modeling based on Large Eddy Simulation (LES). The aim of this paper is twofold: on one hand to improve the general understanding of blood flow in the human LA in normal conditions; on the other, to analyse the effects of VMS-LES models on a situation of blood flow which is neither laminar, nor fully turbulent, but rather transitional as in LA. Our conclusion is that the VMS-LES model is better suited to capture transitional effects than the standard SUPG stabilization method.

Keywords: Left Atrium Hemodynamics, Finite Element method, VMS-LES, SUPG, Transition to Turbulence

*Corresponding author

Email address: alberto.zingaro@polimi.it (Alberto Zingaro)

1. Introduction

In Western Countries, cardiovascular related diseases represent nowadays the first cause of death in the adult population [1]. Non-invasive experimental techniques, such as phase-contrast magnetic resonance imaging (PC-MRI) and computational tomography (CT) scans, allow to inspect the blood fluid-dynamics and displacement of blood vessels. These methods are widely used to better understand the complex physiology of the cardiovascular system as well as to investigate pathological conditions [2, 3]. Cardiovascular diseases diagnosis can also be assessed through 4D flow magnetic resonance imaging (4D flow MRI) [49], a tool which provides 3D visualization of the blood flow along time. Differently from standard experimental techniques [4, 5], 4D flow MRI allows to measure hemodynamics indicators as the wall shear stress (WSS) [48]. However, such imaging based techniques - both standard and more advanced - do not allow to recover the spatial and temporal fine scales of these flows. Hence, they might not accurately catch typical flows features as small coherent structures, recirculation regions and possible regions of transition to turbulence, as pointed out in [48]. For the aforementioned reasons, mathematical modeling and numerical simulations are largely employed to complement the available imaging techniques in an effort to better understand the physiology and pathology of the cardiovascular system [6, 7].

Literature is abundant concerning the fluid dynamics of the whole circulatory system, the study of heart valves, specific arteries and biomedical devices [6, 7, 8, 9, 10, 11, 12, 45, 46, 47]. By far, the most studied part of the heart is the left ventricle (LV) that has been considered from the electro-mechanical and fluid dynamical viewpoints, both for idealized and patient-specific data [8, 13, 14, 44, 43]. The LA is far less investigated, at least in normal conditions [15, 16, 29, 62]. Understanding the blood flow behavior in the LA can shed light on its functioning in physiological conditions and can be also regarded as a valuable step towards the study of the complete left heart.

Idealized geometries for the numerical simulation of blood flows offers the possibility of building a parametrized model that allows to obtain medical indicators for several patients without the need of performing expensive patient-specific simulations. To take into account the large geometrical inter-patient variability, an accurate idealized computational model of the LA can be parametrized based on patient-specific image acquisitions. Another motivation behind the use of an idealized geometry with a prescribed kinematics, which we deduce from the Wiggers diagram [41, 42], lays in the fact that patient-specific data for the atria in normal (physiological) conditions are scarce. Moreover, even if good quality kinematics images of the LA may become available, these would be typically acquired in individuals affected by pathological conditions, such as atrial fibrillation [29].

An open issue in the blood fluid dynamics is whether a transition to turbulence occurs whenever the blood velocity increases and the interactions among vortices are strong. The Navier-Stokes equations are in principle suitable to model both transitional and turbulent flows. However, the spatial and temporal resolutions required to fully capture the details of the flow features through a Direct Numerical Simulation (DNS) for the discretized Navier-Stokes equations would require prohibitive computational resources [18]. For this reason, usually a turbulence model is employed, like e.g. the Reynolds Averaged Navier-Stokes

equations (RANS models) and the Large Eddy Simulation (LES models) [18, 19, 20].

From a theoretical point of view, in a fluid flow, it is possible to distinguish the eddies on the basis of their kinetic energy [18, 21]. The distribution of the kinetic energy as a function of the eddy length scale (or wave number k, when a Fourier transform is applied to the energy spectrum) follows some well established findings in homogeneous and isotropic turbulence, such as the $k^{-5/3}$ rule for the energy spectrum in the inertial range [18, 21]. In RANS models one solves for an average flow field in which only the large scale eddies containing the highest energy are considered, while the effect of the inertial range and of the fine scales is accounted by an extra term, called Reynolds stress, to be added to the momentum balance equation of the Navier-Stokes equations [18, 21]. When using isotropic models, the overall effect of the Reynolds stress term is to increase the viscosity of the fluid with a turbulent viscosity that is added to the physical one. RANS models may become too dissipative and yielding to unrealistic flows when used in transitional or even laminar conditions. On the other hand, LES models aim at solving the large eddies of the flow in the whole inertial range, while modeling the effect of the fine scale dissipative eddies. Stabilization methods of the Navier-Stokes equations to obtain a solution inf-sup stable and free of numerical instabilities evolved towards the formulation of a Variational Multiscale (VMS) framework, contextually yielding a LES model [22, 50, 51, 52, 53, 54].

In this work, we develop a computational model of the human LA based on the incompressible Navier-Stokes equations expressed in the ALE formulation; specifically, we prescribe a law of contraction and relaxation of the LA coherent with the features of the cardiac cycle. We purposely use the VMS-LES model developed in [22] and later extended in [23] to stabilize the numerical solution of the Navier-Stokes equations in ALE formulation and to simultaneously account for turbulence modeling, see e.g. [24]. In particular, the formulation of [23] considers space discretization based on Finite Element Method (FEM) [56, 55] and time discretization based on (Backward Differentiation Formula) BDF [57] and quasi-static approximation of the fine scale solutions. We generate a reference solution on a very fine grid and we compare these results with those obtained with the standard Streamline Upwind Petrov-Galerkin (SUPG) and with the VMS-LES stabilization method [23]. We actually show that the two approaches exhibit similar results in terms of total kinetic energy and enstrophy, and as the mesh becomes finer, the effects of the chosen LES model are less evident, as expected. However, remarkable differences are observed on the fluctuating kinetic energy, especially for the coarsest mesh used, revealing that the VMS-LES formulation is better suited at capturing the transitional blood flow features typically developing in the LA. Our numerical study allows a full characterization of blood flow in the LA in normal conditions. Several meaningful fluid dynamics indicators are also provided.

The outlook of the paper is as follows: in Section 2 we recall the mathematical model, the numerical methods and the LA model that we propose based on physiological data. In Section 3 we present the three mesh levels adopted, while in Section 4 we report and comment the numerical results obtained from the simulation run on the fine mesh (reference solution) in terms of phase-averaged flow properties. Moreover, we perform a mesh converge study along with a comparison between SUPG and VMS-LES stabilization techniques. Finally, conclusions are drawn in Section 5.

2. Mathematical model and numerical methods

In this section we first review the Navier-Stokes equations in ALE framework, then we introduce our numerical methods and the turbulence models. Finally, we discuss the boundary conditions and the LA volume variation in time based on physiological data.

2.1. The Navier-Stokes equations in ALE formulation and its numerical approximation

In large vessels, as well as in the heart chambers, blood behaves as a Newtonian incompressible fluid and the presence of small particles suspended and carried by the plasma can be neglected. In moving domains the Navier-Stokes equations can be reformulated in an Arbitrary Lagrangian Eulerian (ALE) framework with a mesh-moving technique [25, 26]. In this work, we do not study the interactions between the fluid and the endocardium, but we consider that the solid-fluid interface has a prescribed velocity, which is equal to the fluid one with no-slip conditions on the wall. Moreover, we use a standard harmonic extension of the displacement in the fluid domain in order to maintain a good mesh quality while moving it without the need of remeshing [26].

2.1.1. The Navier-Stokes equations in ALE framework

Let $\Omega_t \subset \mathbb{R}^d$ be the fluid domain at a specific time instant $t > 0$, provided with a sufficiently regular boundary Γ_t oriented by outward pointing normal unit vector $\hat{\boldsymbol{n}}$. We denote as Γ_t^D and Γ_t^N the portions of the boundary where respectively Dirichlet and Neumann type boundary conditions are prescribed, with $\Gamma_t = \overline{\Gamma_t^D} \cup \overline{\Gamma_t^N}$ and $\overset{\circ}{\Gamma}{}_t^D \cap \overset{\circ}{\Gamma}{}_t^N = \emptyset$. Let $\boldsymbol{u}$ be the fluid velocity and p be the pressure field. The incompressible Navier-Stokes equations in ALE framework read:

$$\nabla \cdot \boldsymbol{u} = 0 \qquad \text{in } \Omega_t \times (0,T], \tag{1}$$

$$\rho \frac{\hat{\partial} \boldsymbol{u}}{\partial t} + \rho \left(\left(\boldsymbol{u} - \boldsymbol{u}^{\mathrm{ALE}} \right) \cdot \nabla \right) \boldsymbol{u} - \nabla \cdot \boldsymbol{\sigma}(\boldsymbol{u}, p) = \boldsymbol{f} \qquad \text{in } \Omega_t \times (0,T], \tag{2}$$

$$\boldsymbol{u} = \boldsymbol{g} \qquad \text{on } \Gamma_t^D \times (0,T], \tag{3}$$

$$\boldsymbol{\sigma}(\boldsymbol{u}, p)\hat{\boldsymbol{n}} = \boldsymbol{h} \qquad \text{on } \Gamma_t^N \times (0,T], \tag{4}$$

$$\boldsymbol{u} = \boldsymbol{u}_0 \qquad \text{in } \Omega_0 \times \{0\}. \tag{5}$$

In particular, $\dfrac{\hat{\partial} \boldsymbol{u}}{\partial t} = \dfrac{\partial \boldsymbol{u}}{\partial t} + (\boldsymbol{u}_{\mathrm{ALE}} \cdot \nabla)\boldsymbol{u}$ is the ALE derivative, ρ the fluid density and $\boldsymbol{\sigma}(\boldsymbol{u}, p)$ the total stress tensor defined for Newtonian, incompressible and viscous fluids as

$$\boldsymbol{\sigma}(\boldsymbol{u}, p) = -p\boldsymbol{I} + 2\mu\boldsymbol{\varepsilon}(\boldsymbol{u}), \tag{6}$$

being μ the dynamic viscosity and $\boldsymbol{\varepsilon}(\boldsymbol{u})$ the strain-rate tensor defined as

$$\boldsymbol{\varepsilon}(\boldsymbol{u}) = \frac{1}{2}\left(\nabla \boldsymbol{u} + (\nabla \boldsymbol{u})^T \right). \tag{7}$$

The function $\boldsymbol{f}$ is the forcing term, $\boldsymbol{g}$ and $\boldsymbol{h}$ are Dirichlet and Neumann data, $\boldsymbol{u}_0$ the initial condition. We prescribe a velocity $\boldsymbol{g}^{\mathrm{ALE}}$ on the whole boundary Γ_t and we recover $\boldsymbol{u}^{\mathrm{ALE}}$ in the whole domain at each time through an harmonic extension:

$$\begin{aligned} -\nabla \cdot \left(\boldsymbol{K}\nabla \boldsymbol{u}^{\mathrm{ALE}}\right) &= \boldsymbol{0} \qquad \text{in } \Omega_t \times (0,T], \\ \boldsymbol{u}^{\mathrm{ALE}} &= \boldsymbol{g}^{\mathrm{ALE}} \quad \text{on } \Gamma_t \times (0,T], \end{aligned} \tag{8}$$

where $\boldsymbol{K}$ is a positive-definite tensor that can be properly set to better tune the harmonic extension operator, for example depending on the local spatial scales as done in [26]. Finally, the domain displacement $\boldsymbol{d}(\boldsymbol{x},t)$ is obtained integrating over time the ALE velocity:

$$\boldsymbol{d}(\boldsymbol{x},t) = \int_0^t \boldsymbol{u}^{\mathrm{ALE}}(\boldsymbol{x},\tau)d\tau\,. \tag{9}$$

We introduce the the infinite dimensional function spaces:

$$\mathcal{V}_{\boldsymbol{g}} := \{\boldsymbol{v} \in [H^1(\Omega_t)]^d : \boldsymbol{v} = \boldsymbol{g} \text{ on } \Gamma_t^D\}, \tag{10}$$

$$\mathcal{Q} := L^2(\Omega_t), \tag{11}$$

to define the weak formulation of the Navier-Stokes equations in ALE framework, which reads:

given $\boldsymbol{u}_0$, for any $t \in (0,T]$, find $(\boldsymbol{u},p) \in \mathcal{V}_{\boldsymbol{g}} \times \mathcal{Q}$ such that:

$$\begin{aligned} \left(\boldsymbol{v}, \rho\frac{\hat{\partial}\boldsymbol{u}}{\partial t}\right) + \left(\boldsymbol{v}, \rho(\boldsymbol{u}-\boldsymbol{u}^{\mathrm{ALE}})\cdot\nabla\boldsymbol{u}\right) + (\nabla\boldsymbol{v}, \mu\nabla\boldsymbol{u}) - (\nabla\cdot\boldsymbol{v}, p) + (q, \nabla\cdot\boldsymbol{u}) = \\ (\boldsymbol{v},\boldsymbol{f}) + (\boldsymbol{v},\boldsymbol{h})_{\Gamma_t^N}\,, \qquad \text{for all } (\boldsymbol{v},q) \in \mathcal{V}_{\boldsymbol{0}} \times \mathcal{Q}. \end{aligned} \tag{12}$$

We have denoted with $(\cdot,\cdot)$ and $(\cdot,\cdot)_{\Gamma_t^N}$ the L^2 inner product with respect to Ω_t and Γ_t^N respectively.

2.1.2. Numerical methods and turbulence modeling

For the space discretization of Eq. (12), we introduce a finite element (FE) discretization with piecewise Lagrange polynomials of degree $r \geq 1$. The function space of the FE is $X_r^h = \{v^h \in C^0(\overline{\Omega}_t) : v^h|_K \in \mathbb{P}_r, \forall K \in \mathcal{T}_h\}$, being $\mathcal{T}_h$ a triangulation of Ω_t and h the diameter of the grid element $K \in \mathcal{T}_h$.

In the variational multiscale method, a direct-sum decomposition of the spaces $\mathcal{V}_{\boldsymbol{g}}$, $\mathcal{V}_{\boldsymbol{0}}$ and $\mathcal{Q}$ is assumed as [22, 23]

$$\mathcal{V}_{\boldsymbol{g}} = \mathcal{V}_{\boldsymbol{g}}^h \oplus \mathcal{V}_{\boldsymbol{g}}'\,, \qquad \mathcal{V}_{\boldsymbol{0}} = \mathcal{V}_{\boldsymbol{0}}^h \oplus \mathcal{V}_{\boldsymbol{0}}'\,, \qquad \mathcal{Q} = \mathcal{Q}^h \oplus \mathcal{Q}'. \tag{13}$$

In particular, $\mathcal{V}_{\boldsymbol{g}}^h$, $\mathcal{V}_{\boldsymbol{0}}^h$, $\mathcal{Q}^h$ are finite dimensional spaces associated to the FE dicretization, whereas $\mathcal{V}_{\boldsymbol{g}}'$, $\mathcal{V}_{\boldsymbol{0}}'$, $\mathcal{Q}'$ infinite dimensional ones, with $\mathcal{V}_{\boldsymbol{g}}^h = \mathcal{V}_{\boldsymbol{g}} \cap [X_r^h]^d$, $\mathcal{V}_{\boldsymbol{0}}^h = \mathcal{V}_{\boldsymbol{0}} \cap [X_r^h]^d$ and $\mathcal{Q}^h = \mathcal{Q} \cap [X_r^h]^d$. In this way, we introduce an a-priori splitting of the solution into coarse and fine scales, thus every function can be written as:

$$\boldsymbol{u} = \boldsymbol{u}^h + \boldsymbol{u}'\,, \qquad p = p^h + p'\,, \qquad \boldsymbol{v} = \boldsymbol{v}^h + \boldsymbol{v}'\,, \qquad q = q^h + q'\,.$$

By decomposing (12) into coarse and fine scale equations and integrating by parts the fine scale terms into the coarse scale equations, we obtain the coarse equations [22, 23]. Since the fine scales are still defined in an infinite dimensional space, we model them adopting a quasi-static approach as [22, 23]:

$$\boldsymbol{u}' \simeq -\tau_{\mathrm{M}}(\boldsymbol{u}^h)\boldsymbol{r}_{\mathrm{M}}(\boldsymbol{u}^h, p^h) \tag{14}$$

$$p' \simeq -\tau_{\mathrm{C}}(\boldsymbol{u}^h) r_{\mathrm{C}}(\boldsymbol{u}^h), \tag{15}$$

being $\boldsymbol{r}_{\mathrm{M}}(\boldsymbol{u}^h, p^h)$ and $r_{\mathrm{C}}(\boldsymbol{u}^h)$ the strong residuals of (2) and (1) defined respectively as:

$$\boldsymbol{r}_{\mathrm{M}}(\boldsymbol{u}^h, p^h) = \rho\frac{\hat{\partial}\boldsymbol{u}^h}{\partial t} + \rho\left(\left(\boldsymbol{u}^h - \boldsymbol{u}^{\mathrm{ALE}}\right)\cdot\nabla\right)\boldsymbol{u}^h - \nabla\cdot\boldsymbol{\sigma}(\boldsymbol{u}^h, p^h) - \boldsymbol{f} \tag{16}$$

$$r_{\mathrm{C}}(\boldsymbol{u}^h) = \nabla\cdot\boldsymbol{u}^h \tag{17}$$

The stabilization parameters are chosen as in [22, 23]:

$$\tau_{\mathrm{M}}(\boldsymbol{u}^h) = \left(\frac{\rho^2}{\Delta t^2} + \rho^2\left(\boldsymbol{u}^h - \boldsymbol{u}^{\mathrm{ALE}}\right)\cdot\tilde{\boldsymbol{G}}(\boldsymbol{u}^h - \boldsymbol{u}^{\mathrm{ALE}}) + C_r\mu^2\tilde{\boldsymbol{G}} : \tilde{\boldsymbol{G}}\right)^{-\frac{1}{2}}, \tag{18}$$

$$\tau_{\mathrm{C}}(\boldsymbol{u}^h) = \left(\tau_M(\boldsymbol{u}^h)\tilde{\boldsymbol{g}}\cdot\tilde{\boldsymbol{g}}\right)^{-1}, \tag{19}$$

being Δt the time step that will be used for the time discretization and $C_r = 15\cdot 2^r$ is a constant obtained by an inverse inequality depending on the polynomial degree r [22, 23]. Moreover, $\tilde{\boldsymbol{G}}$ is the metric tensor and $\tilde{\boldsymbol{g}}$ the metric vector:

$$\tilde{G}_{ij} = \sum_{k=1}^{d}\frac{\partial\xi_k}{\partial x_i}\frac{\partial\xi_k}{\partial x_j}, \quad \tilde{g}_i = \sum_{j=1}^{d}\frac{\partial\xi_j}{\partial x_i}, \tag{20}$$

whereas we denote with $\boldsymbol{x} = \{x_i\}_{i=1}^d$ the coordinates of the mesh element K in the physical space and with $\boldsymbol{\xi} = \{\xi_i\}_{i=1}^d$ the coordinates of element $\hat{K}$ in the parametric space. Let $\boldsymbol{x} = \boldsymbol{x}(\boldsymbol{\xi}) : \hat{K} \to K$ be a continuous and differentiable mapping from the parametric to the physical space, with a continuously differentiable inverse. $\frac{\partial\boldsymbol{\xi}}{\partial\boldsymbol{x}}$ in Eq. (20) is the inverse Jacobian of the mapping [22].

The semi-discrete variational multiscale formulation with LES modeling of the Navier-Stokes equations in ALE framework reads:

given $\boldsymbol{u}_0$, for any $t \in (0,T]$, find $(\boldsymbol{u}^h, p^h) \in \mathcal{V}_{\boldsymbol{g}}^h \times Q^h$ such that:

$$
\begin{aligned}
&\left(\boldsymbol{v}^h, \rho\frac{\hat{\partial}\boldsymbol{u}^h}{\partial t}\right) + \left(\boldsymbol{v}^h, \rho\left((\boldsymbol{u}^h - \boldsymbol{u}^{\mathrm{ALE}})\cdot\nabla\right)\boldsymbol{u}^h\right) + \left(\nabla\boldsymbol{v}^h, \mu\nabla\boldsymbol{u}^h\right) - \left(\nabla\cdot\boldsymbol{v}^h, p^h\right) + \left(q^h, \nabla\cdot\boldsymbol{u}^h\right)\\
&+ \underbrace{\left(\rho(\boldsymbol{u}^h - \boldsymbol{u}^{\mathrm{ALE}})\cdot\nabla\boldsymbol{v}^h + \nabla q^h,\, \tau_{\mathrm{M}}(\boldsymbol{u}^h)\boldsymbol{r}_{\mathrm{M}}(\boldsymbol{u}^h, p^h)\right) + \left(\nabla\cdot\boldsymbol{v}^h, \tau_{\mathrm{C}}(\boldsymbol{u}^h) r_{\mathrm{C}}(\boldsymbol{u}^h)\right)}_{\text{(I)}}\\
&+ \underbrace{\left(\rho\boldsymbol{u}^h\cdot(\nabla\boldsymbol{v}^h)^T, \tau_{\mathrm{M}}(\boldsymbol{u}^h)\boldsymbol{r}_{\mathrm{M}}(\boldsymbol{u}^h, p^h)\right)}_{\text{(II)}}\\
&- \underbrace{\left(\rho\nabla\boldsymbol{v}^h, \tau_{\mathrm{M}}(\boldsymbol{u}^h)\boldsymbol{r}_{\mathrm{M}}(\boldsymbol{u}^h, p^h)\otimes\tau_{\mathrm{M}}(\boldsymbol{u}^h)\boldsymbol{r}_{\mathrm{M}}(\boldsymbol{u}^h, p^h)\right)}_{\text{(III)}} =\\
&\left(\boldsymbol{v}^h, \boldsymbol{f}\right) + \left(\boldsymbol{v}^h, \boldsymbol{h}\right)_{\Gamma_t^N}, \quad \text{for all } (\boldsymbol{v}^h, q^h) \in \mathcal{V}_{\boldsymbol{0}}^h \times \mathcal{Q}^h.
\end{aligned}
\tag{21}
$$

In Eq. (21), the first and last rows contain integrals of the standard Navier-Stokes equations in ALE framework (see Eq. (12)), the term (I) accounts for SUPG stabilization term, (II) is a stabilization term due to the VMS model, and (III) is the LES term, which models the Reynolds stress term.

We use Backward Euler Method to discretize the problem in time and we extrapolate $\boldsymbol{u}^h$ in the non-linear terms by means of the Newton-Gregory backward polynomials of order one. This yields a single linear problem at each time step. For more details on this implementation and on its strengths and limitations, the interested reader can see [23].

We partition the time interval into N_t subintervals of equal size $\Delta t = \frac{T}{N_t}$, with $t_n = n\Delta t$ and we denote with the subscript n quantities related to the time step n, with $n = 0, \ldots, N_t$. The fully discretized linearized semi-implicit VMS-LES formulation of the Navier-Stokes equations in ALE framework with Backward Euler Method as time integration method reads:

Given $\boldsymbol{u}_n^h$, for any $n = 0, \ldots, N_t - 1$, find $(\boldsymbol{u}_{n+1}^h, p_{n+1}^h) \in \mathcal{V}_g^h \times \mathcal{Q}^h$ such that:

$$
\begin{aligned}
&\left(\boldsymbol{v}^h, \rho\frac{\boldsymbol{u}_{n+1}^h}{\Delta t}\right)_{\Omega_{n+1}} + \left(\boldsymbol{v}^h, \rho(\boldsymbol{u}_n^h - \boldsymbol{u}_{n+1}^{\mathrm{ALE}})\cdot\nabla\boldsymbol{u}_{n+1}^h\right)_{\Omega_{n+1}} + \left(\nabla\boldsymbol{v}^h, \mu\nabla\boldsymbol{u}_{n+1}^h\right)_{\Omega_{n+1}}\\
&- \left(\nabla\cdot\boldsymbol{v}^h, p_{n+1}^h\right)_{\Omega_{n+1}} + \left(q^h, \nabla\cdot\boldsymbol{u}_{n+1}^h\right)_{\Omega_{n+1}}\\
&+ \left(\rho(\boldsymbol{u}_n^h - \boldsymbol{u}_{n+1}^{\mathrm{ALE}})\cdot\nabla\boldsymbol{v}^h + \nabla q^h,\, \tau_{\mathrm{M}}(\boldsymbol{u}_{n+1}^h)\boldsymbol{r}_{\mathrm{M}}(\boldsymbol{u}_{n+1}^h, p_{n+1}^h)\right)_{\Omega_{n+1}} + \left(\nabla\cdot\boldsymbol{v}^h, \tau_{\mathrm{C}}(\boldsymbol{u}_{n+1}^h) r_{\mathrm{C}}(\boldsymbol{u}_{n+1}^h)\right)_{\Omega_{n+1}}\\
&+ \left(\rho(\boldsymbol{u}_n^h - \boldsymbol{u}_{n+1}^{\mathrm{ALE}})\cdot(\nabla\boldsymbol{v}^h)^T, \tau_{\mathrm{M}}(\boldsymbol{u}_{n+1}^h)\boldsymbol{r}_{\mathrm{M}}(\boldsymbol{u}_{n+1}^h, p_{n+1}^h)\right)_{\Omega_{n+1}}\\
&- \left(\rho\nabla\boldsymbol{v}^h, \tau_{\mathrm{M}}(\boldsymbol{u}_{n+1}^h)\boldsymbol{r}_{\mathrm{M}}(\boldsymbol{u}_n^h, p_n^h)\otimes\tau_{\mathrm{M}}(\boldsymbol{u}_{n+1}^h)\boldsymbol{r}_{\mathrm{M}}(\boldsymbol{u}_{n+1}^h, p_{n+1}^h)\right)_{\Omega_{n+1}}\\
&= \left(\boldsymbol{v}^h, \boldsymbol{f}_{n+1}\right)_{\Omega_{n+1}} + \left(\boldsymbol{v}^h, \boldsymbol{h}_{n+1}\right)_{\Gamma_{n+1}^N} + \left(\boldsymbol{v}^h, \rho\frac{\boldsymbol{u}_n^h}{\Delta t}\right)_{\Omega_n} \quad \text{for all } (\boldsymbol{v}^h, q^h) \in \mathcal{V}_0^h \times \mathcal{Q}^h.
\end{aligned}
\tag{22}
$$

The strong residuals, after time discretization, read

$$\boldsymbol{r}_{\mathrm{M}}(\boldsymbol{u}_*^h, p_*^h) = \rho \frac{\boldsymbol{u}_*^h - \boldsymbol{u}_n^h}{\Delta t} + \rho \left(\boldsymbol{u}_n^h - \boldsymbol{u}_{n+1}^{\mathrm{ALE}}\right) \cdot \nabla \boldsymbol{u}_*^h - \mu \Delta \boldsymbol{u}_*^h + \nabla p_*^h - \boldsymbol{f}_{n+1}, \tag{23}$$

$$r_{\mathrm{C}}(\boldsymbol{u}_{n+1}^h) = \nabla \cdot \boldsymbol{u}_{n+1}^h \,. \tag{24}$$

where the subscript $*$ denotes either the time step n or $n+1$, as the residuals appear in Eq. (22).

2.2. Left atrium model

The LA is a chamber located in the left part of the heart anchored on the top of the LV, connected to the pulmonary circulation system through the pulmonary veins (PVs) and to the LV through the mitral valve (MV). The position, size and even the number of PVs is specific to the individual, but there are usually four veins situated in the upper part of the LA in a perpendicular direction with respect to the MV axis. The left atrial appendage (left auricle) is a small secondary cavity located on one side of the LA and connected to the main cavity through an orifice. In Figure 2 we report the geometry of the idealized LA that is used for the numerical simulations, while in Figure 1 we highlight the position of the chamber inside a human torso. The geometry is obtained by filling a LA surface originally built by means of NURBS in [27] with the purpose of modeling the electric potential wavefront. The LA boundary Γ_t is split into six portions: four PVs sections Γ_{PV_i}, $i = 1, \ldots, 4$, the MV section Γ_{MV} and the LA endocardium Γ_{w}. The PVs are considered equal sized and the left atrial appendage is labelled as LAA. The section area of the MV is 6.74 cm^2, while the area of each PV is 0.78 cm^2, if the former were to be considered circular, their diameters would be 2.93 cm and 1 cm respectively.

In physiological conditions, during diastole, blood is ejected from the LA into the LV through the open MV with a first strong ejection and a second weaker one, strengthened by the LA contraction known also as atrial kick. This process is characterized by a volume reduction of about 25% of the initial volume. The first blood ejection from the LA is called Early wave (E-wave) while the atrial kick is also known as After wave (A-wave). During systole the MV closes and the LA is filled with blood coming from the PVs, enlarging to reach the original volume.

In literature, the MV flow has been studied and measured in both physiological and pathological conditions [2, 5, 6, 31, 43, 15]. In Figure 3 (left) we report the inlet (PVs section) and outlet (MV section) flow rates against time. The first peak during diastole is the E-wave, while the second one is the A-wave. During systole the flow through the MV is zero because the valve is closed. The heart cycle considered in this work corresponds to a rest condition at 60 bpm, i.e. the period is equal to $T_{\mathrm{HB}} = 1$ s. The diastole lasts for $T_{\mathrm{dias}} = 0.68$ s and the systole for the remaining $T_{\mathrm{syst}} = 0.32$ s; a whole heartbeat lasts $T_{\mathrm{HB}} = T_{\mathrm{dias}} + T_{\mathrm{syst}}$. We simulate respectively diastole and systole, so that the initial time corresponds to the end systolic phase. The volume variation of the LA is based on the ejection phases, so the volume decrease is modeled in two phases corresponding to the E and A-waves. The LA filling phase is shorter and is accomplished with a continuous rise of the volume. The LA volume as a function of time $V(t)$ is reported in Figure 3 (right) [16].

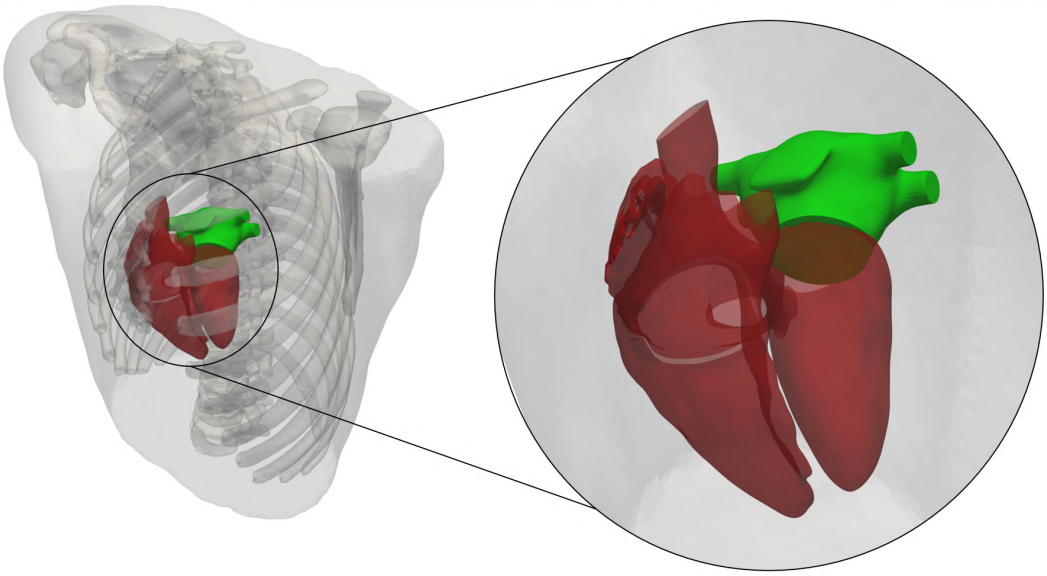

Figure 1: Position of the LA inside the torso. The idealized LA geometry is in green and the remaining heart's chambers in red. The 3D torso model is taken for visualization purposes from the repository CoMMLab [38, 39].

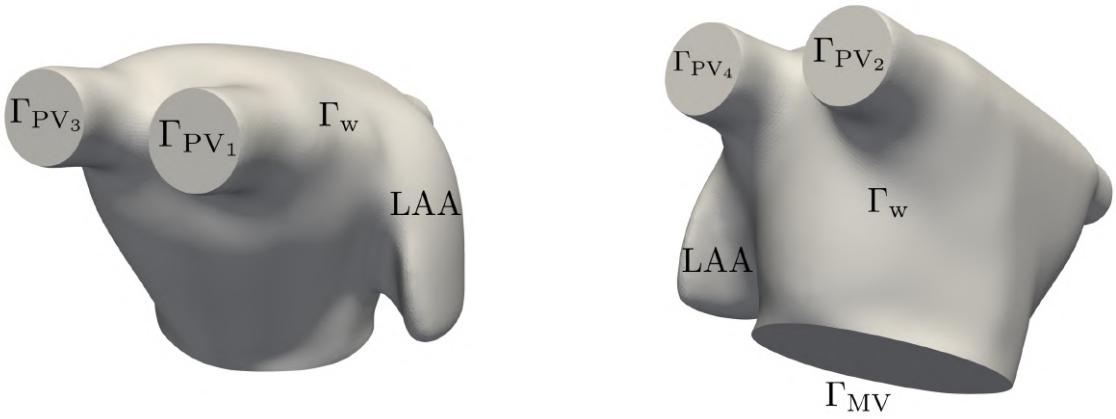

Figure 2: The idealized LA geometry from two different angles. The domain boundary is $\Gamma_t = \Gamma_{\text{w}} \cup \Gamma_{\text{MV}} \cup \left(\bigcup_{i=1}^{4} \Gamma_{\text{PV}_i}\right)$.

As explained in Section 2.1.1, we prescribe a velocity $\boldsymbol{g}^{\text{ALE}}$ on the boundary Γ_t and we extend it harmonically to the whole domain to get the ALE velocity $\boldsymbol{u}^{\text{ALE}}$ (see Eq. (8)). In particular, we compute the ALE velocity on the LA boundary by assuming separation of variables as:

$$\boldsymbol{g}^{\text{ALE}}(\boldsymbol{x}, t) = \boldsymbol{f}^{\text{ALE}}(\boldsymbol{x})\, g^{\text{ALE}}(t) \quad \text{on } \Gamma_t, \tag{25}$$

where $\boldsymbol{f}^{\text{ALE}}(\boldsymbol{x})$ contains the directions of $\boldsymbol{g}^{\text{ALE}}$ and $g^{\text{ALE}}(t)$ is a time-dependent function. We design $\boldsymbol{f}^{\text{ALE}}$ to decrease the wall velocity near the PVs ($\boldsymbol{g}^{\text{ALE}} = \boldsymbol{0}$ on Γ_{PV_i}, $i = 1, \ldots, 4$).

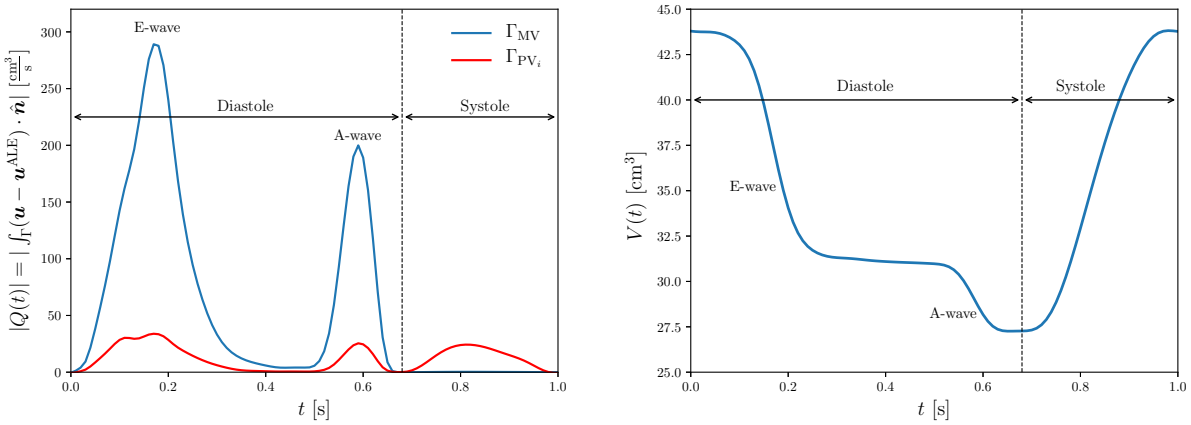

Figure 3: Blood flow through the MV section (Γ_{MV}) and in each PV (Γ_{PV_i}, $i = 1, \dots, 4$) vs. time (left). Idealized LA volume vs. time (right).

Let x_G, y_G, z_G be the coordinates of the LA center of mass (units in cm), we define the function $\boldsymbol{f}^{\text{ALE}}$ as:

$$\boldsymbol{f}^{\text{ALE}}(\boldsymbol{x}) = F(z)((x - x_G)\hat{\boldsymbol{x}} + (y - y_G)\hat{\boldsymbol{y}} + 0.6(z - z_G)\hat{\boldsymbol{z}}), \tag{26}$$

with

$$F(z) = \begin{cases} 0.5 & \text{if } |z - z_G| \in [0, 2.5] \text{ cm}, \\ 0.5\left(\dfrac{2.5 - |z - z_G|}{0.72} + 1\right) & \text{if } |z - z_G| \in [2.5, 3.22] \text{ cm}, \\ 0 & \text{if } |z - z_G| \in [3.22, 10] \text{ cm}. \end{cases} \tag{27}$$

The function F is represented in Figure 4 (left). In order to get the time variation of the prescribed ALE velocity $g^{\text{ALE}}(t)$, we consider the volume variation and we exploit the Reynolds transport theorem (RTT) and Eq. (25):

$$\frac{dV(t)}{dt} = \frac{d}{dt}\int_{\Omega_t} d\Omega \overset{\text{RTT}}{=} \int_{\Gamma_t} \boldsymbol{g}^{\text{ALE}} \cdot \hat{\boldsymbol{n}} d\Gamma \overset{\text{Eq. (25)}}{=} g^{\text{ALE}}(t) \int_{\Gamma_t} \boldsymbol{f}^{\text{ALE}} \cdot \hat{\boldsymbol{n}} d\Gamma, \tag{28}$$

which gives the following definition of g^{ALE}:

$$g^{\text{ALE}}(t) = \frac{1}{\int_{\Gamma_t} \boldsymbol{f}^{\text{ALE}} \cdot \hat{\boldsymbol{n}} d\Gamma} \frac{dV(t)}{dt}. \tag{29}$$

To better appreciate the LA deformation, in Figure 4 (right) we overlap the geometry of the LA in its relaxed and contracted configurations, at the beginning and at the end of diastole, where the maximum LA contraction is met, respectively.

In terms of boundary conditions, during diastole (MV is open), we set a homogeneous Neumann boundary condition on the MV section and we prescribe Poiseuille profiles on the

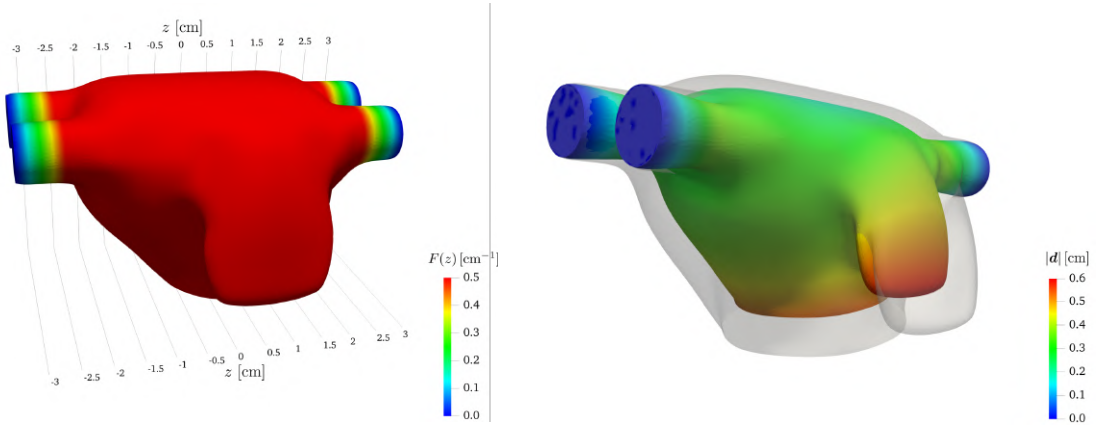

Figure 4: Function $F(z)$ on the LA surface (left). LA geometry at its maximum contraction at end diastole (right): the colors in the deformed geometry highlight the magnitude of the displacement vector.

PVs. We do this using, for each vein, a parabolic velocity profile and imposing the inlet flow-rate Q_{PV_i} $i = 1, \ldots, 4$ that fulfils the mass balance:

$$\sum_{i=1}^{4} |Q_{\mathrm{PV}_i}(t)| = |Q_{\mathrm{MV}}(t)| + \left| \frac{dV(t)}{dt} \right|, \tag{30}$$

whereas the fluxes are defined as:

$$Q_{\mathrm{PV}_i}(t) = \int_{\Gamma_{\mathrm{PV}_i}} \left(\boldsymbol{u} - \boldsymbol{u}^{\mathrm{ALE}} \right) \cdot \hat{\boldsymbol{n}} d\Gamma, \quad i = 1, \ldots, 4, \tag{31}$$

$$Q_{\mathrm{MV}}(t) = \int_{\Gamma_{\mathrm{MV}}} \left(\boldsymbol{u} - \boldsymbol{u}^{\mathrm{ALE}} \right) \cdot \hat{\boldsymbol{n}} d\Gamma. \tag{32}$$

During systole, the MV is closed ($Q_{\mathrm{MV}}(t) = 0$), so we switch the boundary condition on Γ_{MV} to a Dirichlet one to model the closed behaviour of the valve: $\boldsymbol{u} = \boldsymbol{g}^{\mathrm{ALE}}$. The sudden switch of boundary conditions from natural to essential and viceversa – aimed at replicating the rapid closing and opening stages of the MV – may potentially introduce some artifacts on the numerical solution, even if these are negligible in our experience. Furthermore, we use a homogeneous Neumann boundary condition on one of the PVs (Γ_{PV_4}) while keeping a Dirichlet boundary condition with assigned flux given by (30) on the other three. As a matter of fact, numerical oscillations due to the enforcement of the incompressibility constraint in the three remaining inlet sections and Dirichlet boundary conditions in the rest of the boundaries ($\Gamma_{\mathrm{w}} \cup \Gamma_{\mathrm{MV}}$) are strongly reduced with this boundary conditions choice. In addition, we have found that during systole the velocity profile on Γ_{PV_4} resembles a Poiseuille profile. By setting the boundary conditions as explained, we obtain the fluxes through the MV section and through each PV as reported in Figure 3.

Moreover, a backflow stabilization is introduced in all the homogeneous Neumann-type boundary conditions in order to weakly penalize the reverse flow [36]:

$$\boldsymbol{\sigma}(\boldsymbol{u}, p)\hat{\boldsymbol{n}} = \rho(\{\left(\boldsymbol{u} - \boldsymbol{u}^{\mathrm{ALE}}\right) \cdot \hat{\boldsymbol{n}}\}_{-}) \left(\boldsymbol{u} - \boldsymbol{u}^{\mathrm{ALE}}\right) \quad \text{on } \Gamma_t^N, \tag{33}$$

being $\{(\boldsymbol{u}-\boldsymbol{u}^{\mathrm{ALE}})\cdot\hat{\boldsymbol{n}}\}_-$ the negative part of $(\boldsymbol{u}-\boldsymbol{u}^{\mathrm{ALE}})\cdot\hat{\boldsymbol{n}}$:

$$\{(\boldsymbol{u}-\boldsymbol{u}^{\mathrm{ALE}})\cdot\hat{\boldsymbol{n}}\}_- = \begin{cases} (\boldsymbol{u}-\boldsymbol{u}^{\mathrm{ALE}})\cdot\hat{\boldsymbol{n}} & \text{if } (\boldsymbol{u}-\boldsymbol{u}^{\mathrm{ALE}})\cdot\hat{\boldsymbol{n}} < 0, \\ 0 & \text{if } (\boldsymbol{u}-\boldsymbol{u}^{\mathrm{ALE}})\cdot\hat{\boldsymbol{n}} \geq 0. \end{cases} \tag{34}$$

Finally, we summarize in Eq. (35) the whole set of boundary and initial conditions for the modelling of blood flow in the LA.

$$\begin{aligned}
&\boldsymbol{u} = -\frac{|Q_{\mathrm{PV}_i}(t)|}{4|\Gamma_{\mathrm{PV}_i}|}\left(1-\frac{r(\boldsymbol{x})^2}{R_i^2}\right)\hat{\boldsymbol{n}}_i && \text{on } \Gamma_{\mathrm{PV}_i}\times(0,T_{\mathrm{dias}}),\ i=1\ldots,4,\\
&\boldsymbol{\sigma}(\boldsymbol{u},p)\hat{\boldsymbol{n}} = \rho(\{(\boldsymbol{u}-\boldsymbol{u}^{\mathrm{ALE}})\cdot\hat{\boldsymbol{n}}\}_-)\,(\boldsymbol{u}-\boldsymbol{u}^{\mathrm{ALE}}) && \text{on } \Gamma_{\mathrm{MV}}\times(0,T_{\mathrm{dias}}],\\
&\boldsymbol{u} = \boldsymbol{g}^{\mathrm{ALE}} && \text{on } \Gamma_{\mathrm{w}}\times(0,T_{\mathrm{dias}}],\\
&\boldsymbol{u} = -\frac{|Q_{\mathrm{PV}_i}(t)|}{4|\Gamma_{\mathrm{PV}_i}|}\left(1-\frac{r(\boldsymbol{x})^2}{R_i^2}\right)\hat{\boldsymbol{n}}_i && \text{on } \Gamma_{\mathrm{PV}_i}\times(T_{\mathrm{dias}},T_{\mathrm{HB}}],\ i=1\ldots,3,\\
&\boldsymbol{\sigma}(\boldsymbol{u},p)\hat{\boldsymbol{n}} = \rho(\{(\boldsymbol{u}-\boldsymbol{u}^{\mathrm{ALE}})\cdot\hat{\boldsymbol{n}}\}_-)\,(\boldsymbol{u}-\boldsymbol{u}^{\mathrm{ALE}}) && \text{on } \Gamma_{\mathrm{PV}_4}\times(T_{\mathrm{dias}},T_{\mathrm{HB}}],\\
&\boldsymbol{u} = \boldsymbol{g}^{\mathrm{ALE}} && \text{on } \Gamma_{\mathrm{w}}\cup\Gamma_{\mathrm{MV}}\times(T_{\mathrm{dias}},T_{\mathrm{HB}}],\\
&\boldsymbol{u} = \boldsymbol{0} && \text{in } \Omega_0\times\{0\},
\end{aligned} \tag{35}$$

in the Dirichlet inflow boundary condition, $r(\boldsymbol{x}) = |\boldsymbol{x}|$, R_i is the radius of the i–th PV section and $\hat{\boldsymbol{n}}_i$ its outward directed unit vector normal to.

3. Mesh generation

	Mesh	$\mathcal{T}_{h_1}$	$\mathcal{T}_{h_2}$	$\mathcal{T}_{h_3}$
	# elements	575'220	1'711'622	8'344'030
# DOFs ($\mathbb{P}1-\mathbb{P}1$)	$\boldsymbol{u}^h$	291'561	830'517	4'030'227
	p^h	97'187	276'839	1'343'409
	total	388'748	1'107'356	5'373'636
Inner elements	$h_{\min}$ [cm]	0.05	0.05	0.05
	$h_{\max}$ [cm]	0.2	0.1	0.05
Boundary layer	δ_{BL} [cm]	0.05	0.05	0.05
	n_{layers}	3	4	5
	χ_{BL}	0.8	0.8	0.8

Table 1: Details on the three meshes $\mathcal{T}_{h_i}$, $i=1,\ldots,3$: number of elements; number of degrees of freedom (DOFs) using Lagrangian linear elements (for velocity, pressure and total number); minimum and maximum cell size for the inner elements of the mesh; boundary layer: boundary layer thickness δ_{BL}, number of layers n_{layers} and ratio among successive layers' thicknesses χ_{BL}.

.

We generate three meshes, namely a coarse, medium and a fine one, denoted respectively as $\mathcal{T}_{h_1}$, $\mathcal{T}_{h_2}$ and $\mathcal{T}_{h_3}$. As shown in Figure 5 and reported in Table 1, for $\mathcal{T}_{h_1}$ and $\mathcal{T}_{h_2}$, a non-uniform distribution of mesh element size is considered in order to have a well resolved LAA. In particular, we adopt for all mesh levels the same minimum cell-size $h_{\text{min}} = 0.05$ cm in the lower corner of the LAA and we increase it linearly through an appropriate distance function (for $\mathcal{T}_{h_1}$ and $\mathcal{T}_{h_2}$ only). $\mathcal{T}_{h_3}$ instead keeps uniform grid cells sizes $h_{\text{min}} = h_{\text{max}} = 0.05$ cm. Furthermore, in order to accurately catch viscous effects near the wall, we introduce a boundary layer made of n_{layers} layers with linearly variable element thicknesses. In particular, we adopt for all the meshes the same boundary layer thickness $\delta_{\text{BL}} = 0.05$ cm, while we increase the number of layers - going from a mesh level to another - keeping the same ratio among successive layers' thicknesses χ_{BL}. Table 1 lists quantitative information about the three meshes. Mesh generation is performed by exploiting the VMTK library [37, 60]. Meshes are uploaded to a GitLab repository and publicy accessible [63].

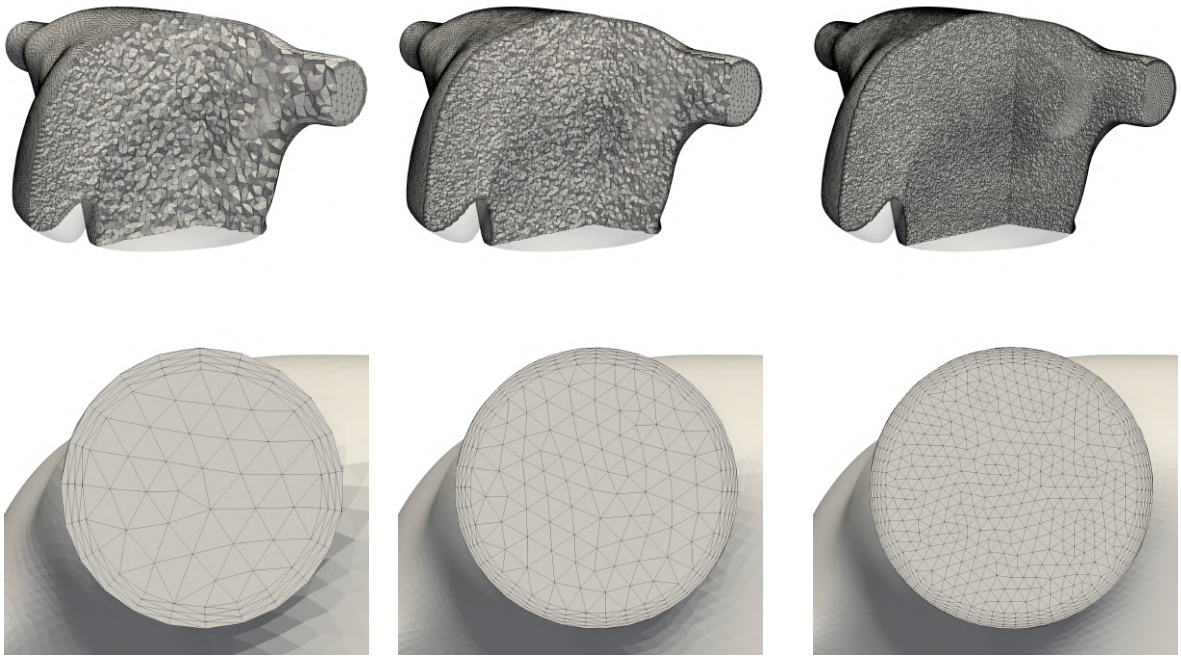

(a) mesh $\mathcal{T}_{h_1}$ (b) mesh $\mathcal{T}_{h_2}$ (c) mesh $\mathcal{T}_{h_3}$

Figure 5: The three meshes $\mathcal{T}_{h_i}$, $i = 1, \ldots, 3$ adopted for the CFD simulations of the idealized LA geometry with a focus on a inlet section.

4. Numerical results and discussion

We report the numerical results obtained perfoming numerical simuluations[1] with the FE library LifeV [28, 58] for the solution of the fluid dynamics in the idealized LA as modeled in Sections 2 and 3.

Blood is set as Newtonian, incompressible and viscous fluid with density $\rho = 1.06$ g/cm^3 and dynamic viscosity $\mu = 0.035$ g/(cm s). For each $\mathcal{T}_{h_i}$, $i = 1, \ldots, 3$, we simulate six heartbeats, starting from the initial condition $\boldsymbol{u}_0 = \boldsymbol{0}$. Due to the periodicity in time of the boundary conditions of the problem, we analyse the output of the numerical simulations with a phase-averaging filter in order to get average quantities on one representative cycle. Furthermore, in order to remove the influence the unphysical initial condition $\boldsymbol{u}_0 = \boldsymbol{0}$, we discard the first two heartbeats. Hence, referring to $N_{\text{HB}} = 4$ heartbeats, with period $T_{\text{HB}} = 1$ s, we introduce the phase-averaging filter for the velocity as:

$$\langle \boldsymbol{u}(\boldsymbol{x}, t) \rangle = \frac{1}{N_{\text{HB}}} \sum_{n=1}^{N_{\text{HB}}} \boldsymbol{u}(\boldsymbol{x}, t + (n-1)T_{\text{HB}}). \tag{36}$$

First, we present the results achieved with the mesh $\mathcal{T}_{h_3}$ using the SUPG stabilization method, which will represent our reference solution. Then, we perform a mesh convergence study using both SUPG and VMS-LES models, comparing the results with the reference solution. Finally, we compare the two methods in terms of fluid dynamics indicators.

4.1. The reference solution

We report the results obtained with the mesh $\mathcal{T}_{h_3}$ by adopting a SUPG stabilization method, with a time step $\Delta t = 6.25 \cdot 10^{-5}$ s. The numerical solution correspondingly obtained is denoted as our reference solution. We remark that the results that will present are referred to the phase-averaged velocity $\langle \boldsymbol{u} \rangle$ which is representative of a heartbeat defined in the time domain $[0, T_{\text{HB}}]$.

In Figure 6, we report the phase-averaged velocity magnitude of the blood on a slice cutting two PVs at six time instants corresponding to the diastolic peak of the E-wave ($t = 0.20$ s), the plateau between E and A-waves ($t = 0.40$ s), the A-wave ($t = 0.60$ s), the beginning of systole ($t = 0.68$ s), the filling phase during systole ($t = 0.80$ s) and the end of systole ($t = 1.00$ s). The peak velocity attained in our simulations is around 90 cm/s during the E-wave. The jets coming from the PVs impact one on each other, as it can be seen at time 0.20 s.

In Figure 7, we report volume rendering of the phase-averaged velocity magnitude at different time instants. The flow shows quite complex features, in particular we observe that the jets impact during the heartbeat in three peculiar instants: the E-wave (Figure 7a), the A-wave (Figure 7b) and during the filling phase of systole (Figure 7e).

[1]Numerical simulations were run on the cluster iHEART (Lenovo SR950 8 x 24-Core Intel Xeon Platinum 8160, 2100 MHz and 1.7TB RAM) available at MOX, Dipartimento di Matematica, Politecnico di Milano. Furthermore, simulations on the mesh $\mathcal{T}_{h_3}$ were run on the cluster GALILEO supercomputer (IBM NeXtScale cluster, 1022 nodes (Intel Broadwell), 2 x 18-Cores Intel Xeon E5-2697 v4 at 2.30 GHz, 36 cores/node, 26.572 cores in total with 128 GB/node) by CINECA.

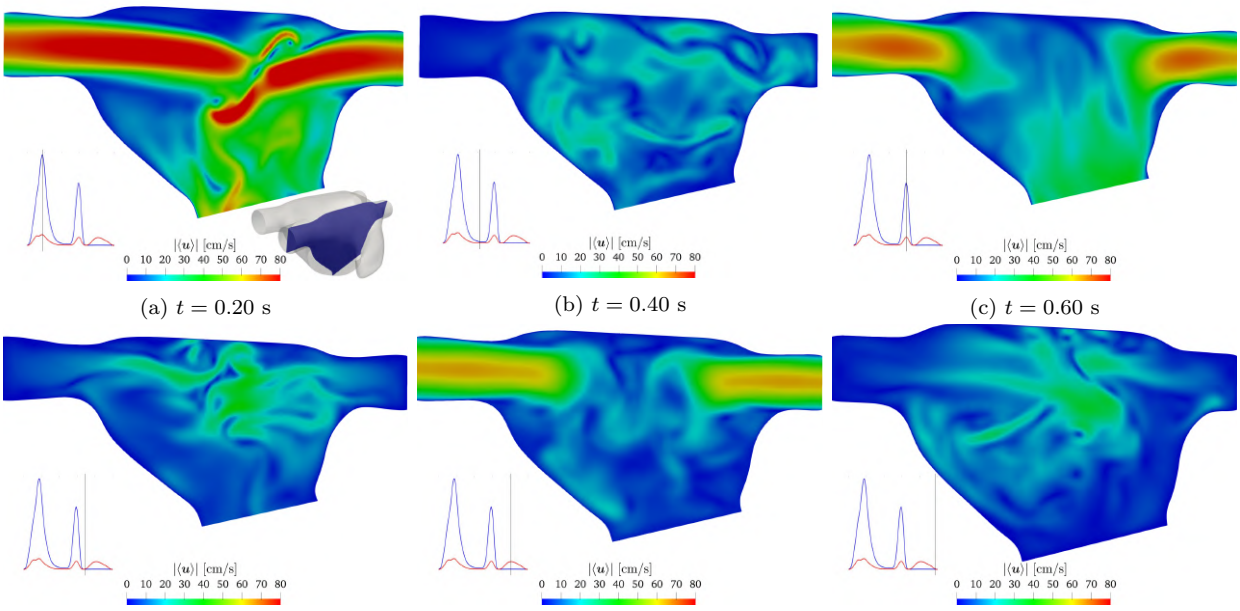

(a) $t = 0.20$ s (b) $t = 0.40$ s (c) $t = 0.60$ s

(d) $t = 0.68$ s (e) $t = 0.80$ s (f) $t = 1.00$ s

Figure 6: Reference solution: phase-averaged velocity magnitude $|\langle \boldsymbol{u} \rangle|$ on a slice cutting two PVs (top-left) at different time instants.

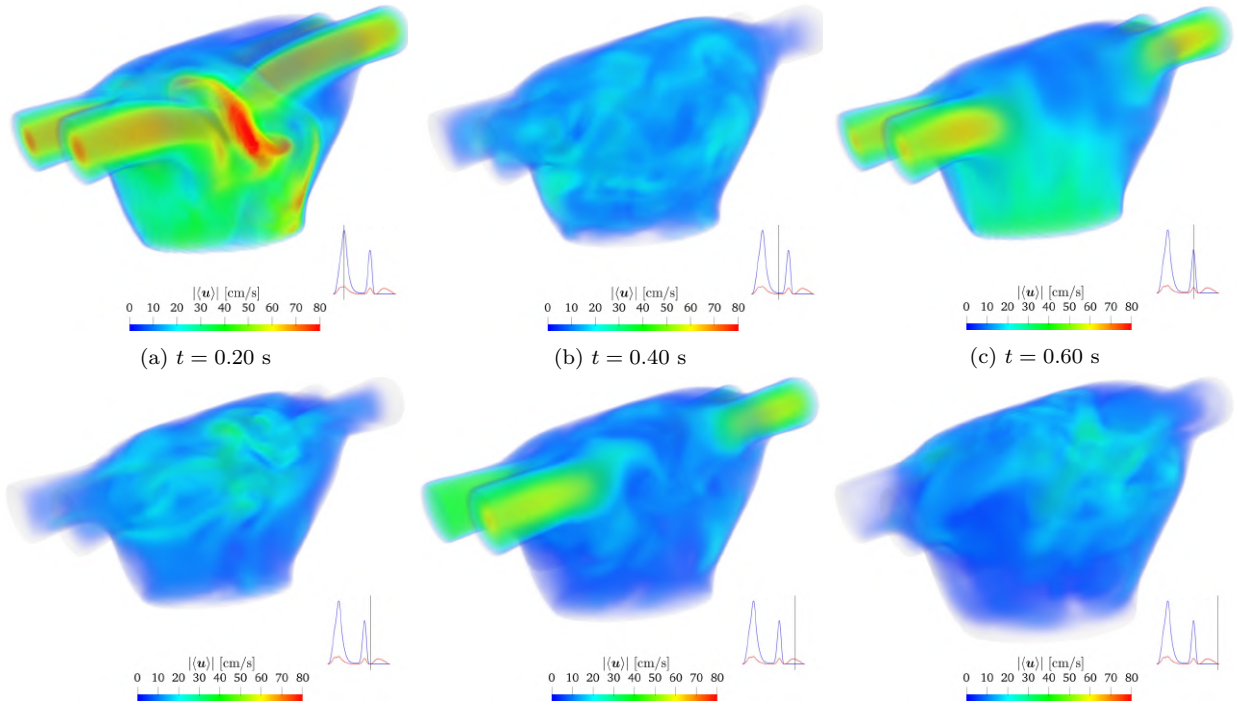

(a) $t = 0.20$ s (b) $t = 0.40$ s (c) $t = 0.60$ s

(d) $t = 0.68$ s (e) $t = 0.80$ s (f) $t = 1.00$ s

Figure 7: Reference solution: volume rendering of phase-averaged velocity magnitude $|\langle \boldsymbol{u} \rangle|$ at different time instants.

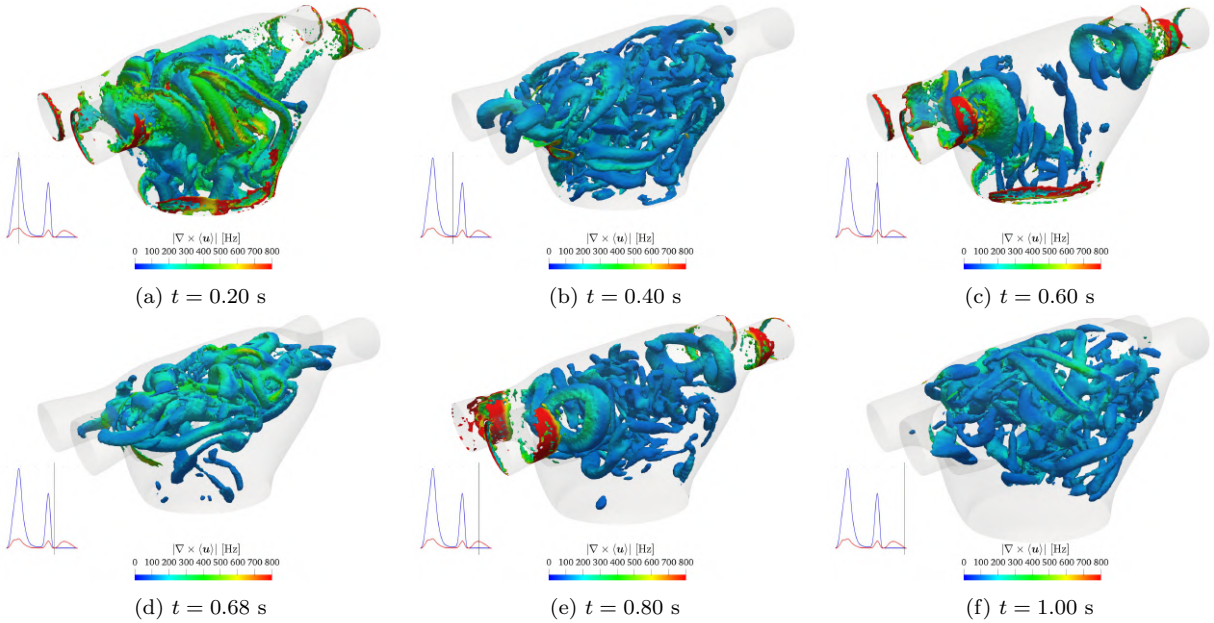

(a) $t = 0.20$ s (b) $t = 0.40$ s (c) $t = 0.60$ s

(d) $t = 0.68$ s (e) $t = 0.80$ s (f) $t = 1.00$ s

Figure 8: Reference solution: isosurfaces of Q-criterion $Q = 2000$ Hz^2 coloured by phase-averaged vorticity magnitude $|\nabla \times \langle \boldsymbol{u} \rangle|$ at different time instants.

We split the velocity gradient $\nabla\langle \boldsymbol{u} \rangle$ into its symmetric $\boldsymbol{\varepsilon}(\langle \boldsymbol{u} \rangle)$ and skew-symmetric $\boldsymbol{\omega}(\langle \boldsymbol{u} \rangle)$ parts:

$$\nabla\langle \boldsymbol{u} \rangle = \frac{1}{2}\left(\nabla\langle \boldsymbol{u} \rangle + (\nabla\langle \boldsymbol{u} \rangle)^T\right) + \frac{1}{2}\left(\nabla\langle \boldsymbol{u} \rangle - (\nabla\langle \boldsymbol{u} \rangle)^T\right) = \boldsymbol{\varepsilon}(\langle \boldsymbol{u} \rangle) + \boldsymbol{\omega}(\langle \boldsymbol{u} \rangle), \tag{37}$$

being respectively the strain-rate tensor and the rotation tensor. In order to identify coherent vortex structures, we introduce the scalar function [59]:

$$Q(\langle \boldsymbol{u} \rangle) = \frac{1}{2}\left(|\boldsymbol{\omega}(\langle \boldsymbol{u} \rangle)|_{\mathrm{F}}^2 - |\boldsymbol{\varepsilon}(\langle \boldsymbol{u} \rangle)|_{\mathrm{F}}^2\right), \tag{38}$$

where $|\cdot|_{\mathrm{F}}$ is the Frobenius norm of a tensor. If $Q(\langle \boldsymbol{u} \rangle) > 0$, the rotation of a fluid element becomes dominant over its stretching: the Q-criterion consists in analysing the isosurfaces of the positive part of $Q(\langle \boldsymbol{u} \rangle)$ [59]. In Figure 8 we plot the isosurfaces corresponding to $Q = 2000$ Hz^2 coloured with the phase-averaged vorticity magnitude $|\nabla \times \langle \boldsymbol{u} \rangle|$. The main feature of this flow is the formation of vortex rings out of the PVs when the blood enters in the LA. These rings mutually interact when the corresponding jets impact and then form structures that become smaller and smaller until disappearing by dissipating their energy. In Figure 8a, we highlight the impact among the strong jets during the E-wave. Then, at time $t = 0.40$ s (Figure 8b), the structures become smaller and they have nearly disappeared as new jet enters at time $t = 0.60$ s (Figure 8c) forming four well visible vortex rings around the PVs sections (A-wave). In the refilling phase of systole ($t = 0.80$ s), the vortex rings are again visible with some residual structures still present at the center of the chamber.

By focusing on the impact during the E-wave, in Figure 9, we show the projection of the phase-averaged vorticity $\nabla \times \langle \boldsymbol{u} \rangle$ on the normal direction of a slice cutting two PVs. We

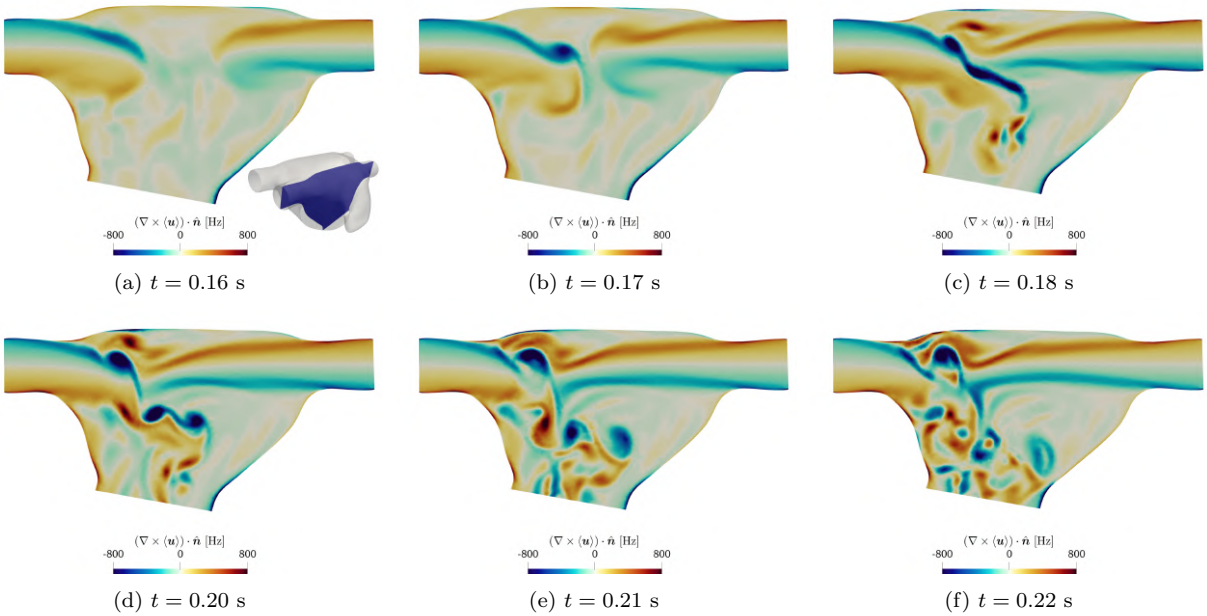

(a) $t = 0.16$ s (b) $t = 0.17$ s (c) $t = 0.18$ s

(d) $t = 0.20$ s (e) $t = 0.21$ s (f) $t = 0.22$ s

Figure 9: Reference solution: projection of the phase-averaged vorticity on the normal direction of a slice cutting two PVs (top-left) $(\nabla \times \langle \boldsymbol{u} \rangle) \cdot \hat{\boldsymbol{n}}$. Results at different time instants in the proximity of the E-wave ($t = 0.20$ s).

observe the formation of shear layers from the PVs (Figure 9a), a early-stage interaction in Figure 9b along with some recirculation regions. Then, from $t = 0.18$ s, we observe perturbed shear layers with a coalescence of vortices and a dispersion of the organized flow pattern previously seen (Figures 9c, 9d). In particular, the vortices breakdown propagates in the rest of the chamber, towards the MV section (Figures 9e, 9f).

The velocity profile at the MV is an interesting output of this computation since it can be used as input for the simulation of the LV hemodynamics [30, 31]. In Figure 10, we report glyphs of velocity vector at the MV section during diastole (i.e. when the MV is open) on a slice coloured with $\langle \boldsymbol{u} \rangle \cdot \hat{\boldsymbol{n}}_{\mathrm{MV}}$, i.e. the scalar product among the phase-averaged velocity and the outward pointing unit vector normal to the MV section. We notice that the velocity profile that we obtain is highly variable in time and, more importantly, the velocity shows a flat profile only at some specific times, such as at $t = 0.10$ s (Figure 10a). Even when the flow is intense, such as at $t = 0.20$ s or $t = 0.60$ s, the velocity profile is never flat but, on the contrary, the presence of vortices located above the MV section produces low velocity regions as shown in Figures 10b and 10f. During the time between the two waves, the integrated outflow is positive, as can be seen in Figures 10c, 10d and 10e, but some recirculating velocities are visible in some spots reaching negative values of $\langle \boldsymbol{u} \rangle \cdot \hat{\boldsymbol{n}}_{\mathrm{MV}} = -15$ cm/s.

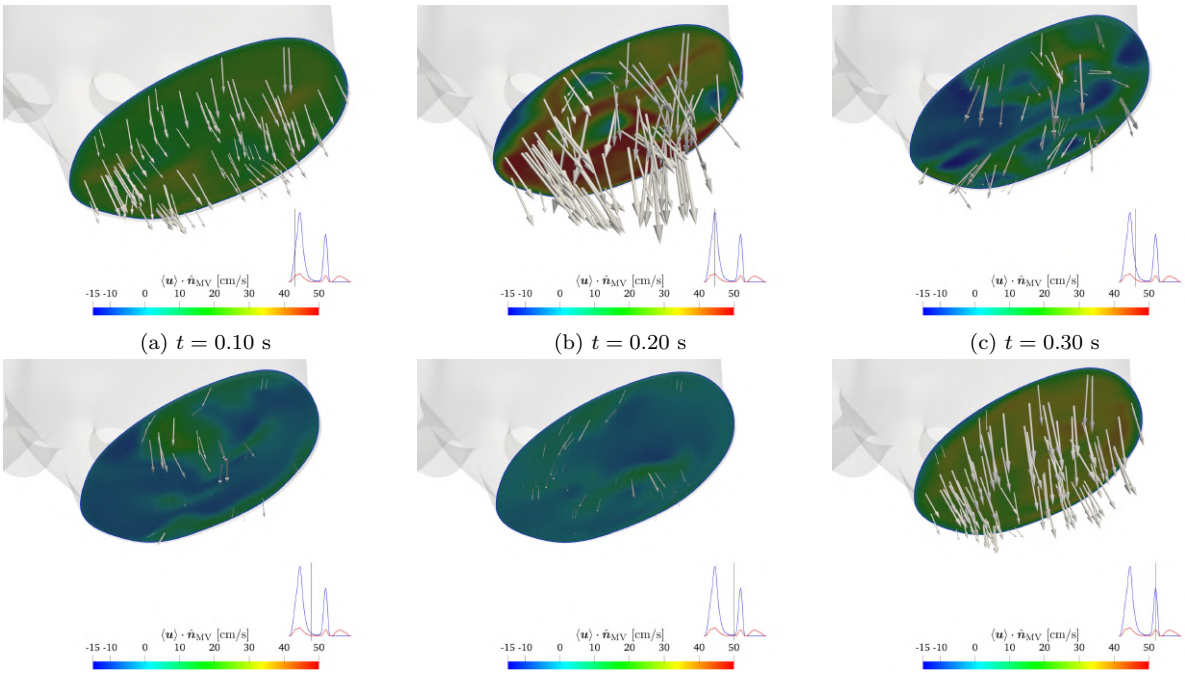

(a) $t = 0.10$ s (b) $t = 0.20$ s (c) $t = 0.30$ s

(d) $t = 0.40$ s (e) $t = 0.50$ s (f) $t = 0.60$ s

Figure 10: Reference solution: glyphs of velocity vector at the MV section during diastole on a slice coloured with $\langle \boldsymbol{u} \rangle \cdot \hat{\boldsymbol{n}}_{\mathrm{MV}}$, i.e. the scalar product among the phase-averaged velocity and the outward pointing unit vector normal to the MV section.

In view of calculating hemodynamic indicators, we define the viscous stress tensor related to the phase-averaged velocity field as

$$\boldsymbol{\tau}(\langle \boldsymbol{u} \rangle) = 2\mu \boldsymbol{\varepsilon}(\langle \boldsymbol{u} \rangle). \tag{39}$$

We compute the vector wall shear stress (**WSS**) on the boundary of the reference configuration Ω_0 (i.e. the LA at the beginning of diastole) as

$$\mathbf{WSS}(\langle \boldsymbol{u} \rangle) = \boldsymbol{\tau}(\langle \boldsymbol{u} \rangle)\hat{\boldsymbol{n}} - (\boldsymbol{\tau}(\langle \boldsymbol{u} \rangle)\hat{\boldsymbol{n}} \cdot \hat{\boldsymbol{n}})\,\hat{\boldsymbol{n}} \quad \text{on } \partial\Omega_0, \tag{40}$$

and the scalar fields time averaged wall shear stress (TAWSS), oscillatory shear index (OSI) and relative residence time (RRT) (see [16, 32, 33]). These indicators are meaningful since endothelial cells and their long-term response affect both the magnitude in the WSS and by its evolution in time. For this reason, they can be used to identify formation of new tissues, plaques and the promoting of neointimal hyperplasia [32]. With the WSS, we compute the TAWSS as the integral over the time period of the magnitude of the **WSS**,

$$\mathrm{TAWSS}(\langle \boldsymbol{u} \rangle) = \frac{1}{T_{\mathrm{HB}}} \int_0^{T_{\mathrm{HB}}} |\mathbf{WSS}(\langle \boldsymbol{u} \rangle)|_2 dt \quad \text{on } \partial\Omega_0, \tag{41}$$

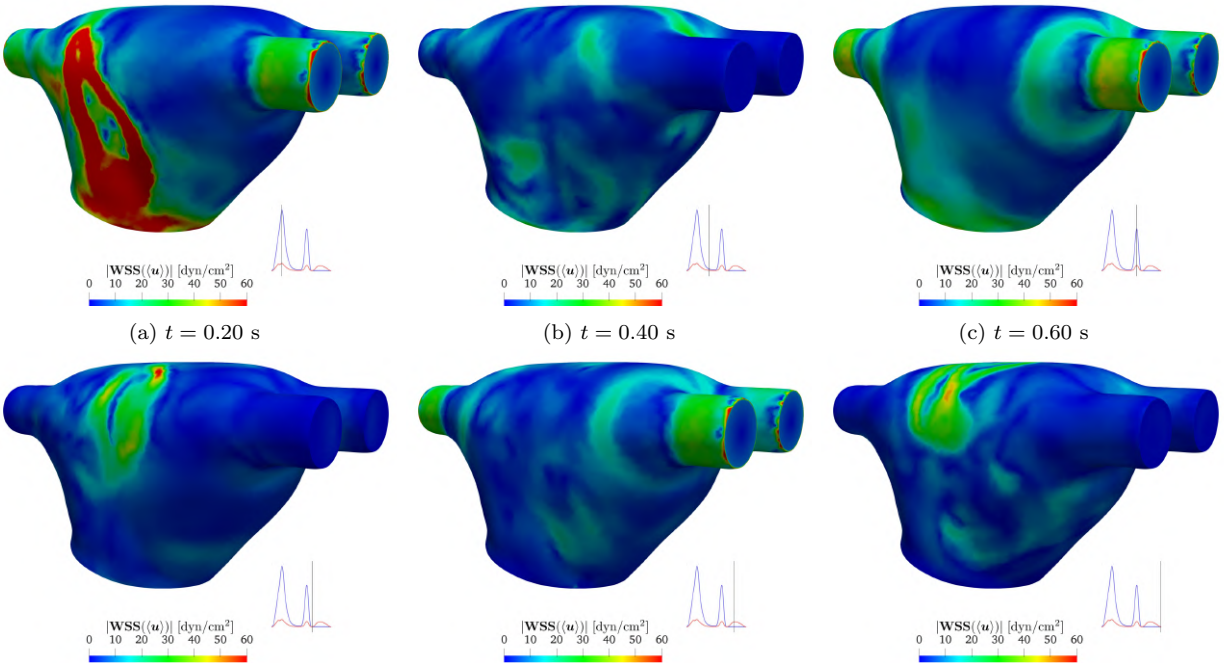

(a) $t = 0.20$ s (b) $t = 0.40$ s (c) $t = 0.60$ s

(d) $t = 0.68$ s (e) $t = 0.80$ s (f) $t = 1.00$ s

Figure 11: Reference solution: wall shear stress (WSS) magnitude at different time instants.

where $|\cdot|_2$ denotes the Euclidean norm of a vector. The OSI is defined as [32]:

$$\mathrm{OSI}(\langle \boldsymbol{u} \rangle) = \frac{1}{2}\left(1 - \frac{\left|\int_0^{T_{\mathrm{HB}}} \mathbf{WSS}(\langle \boldsymbol{u} \rangle) dt\right|_2}{\int_0^{T_{\mathrm{HB}}} |\mathbf{WSS}(\langle \boldsymbol{u} \rangle)|_2 \, dt}\right) \quad \text{on } \partial\Omega_0, \tag{42}$$

and it is higher in regions where the WSS changes much during a heart cycle. Finally, we compute the RRT as in [33]

$$\mathrm{RRT}(\langle \boldsymbol{u} \rangle) = \left((1 - 2\,\mathrm{OSI}(\langle \boldsymbol{u} \rangle)) \frac{1}{T_{\mathrm{HB}}} \int_0^{T_{\mathrm{HB}}} |\mathbf{WSS}(\langle \boldsymbol{u} \rangle)|_2 \, dt\right)^{-1} \quad \text{on } \partial\Omega_0. \tag{43}$$

The RRT is proportional to the residence time of blood particles in the proximity of the wall, and it can be regarded as a convenient fluid dynamics indicator to identify regions where WSS is both low and oscillatory [61].

In Figure 11, we report the WSS magnitude as computed on the surface of the LA at different time instants by using the phase averaged velocity. The largest values are attained during the E-wave in the middle of the surface of the LA, towards the MV.This region corresponds to areas where vortices interact and are pushed towards the LA wall. During the rest of the cycle, the WSS values remain quite small; large values are attained only in the PVs and in the lower part of the LA.

Figure 12 shows the TAWSS on the reference configuration from two different perspectives: low values of the TAWSS are achieved in the LAA, while some peaks can be appre-

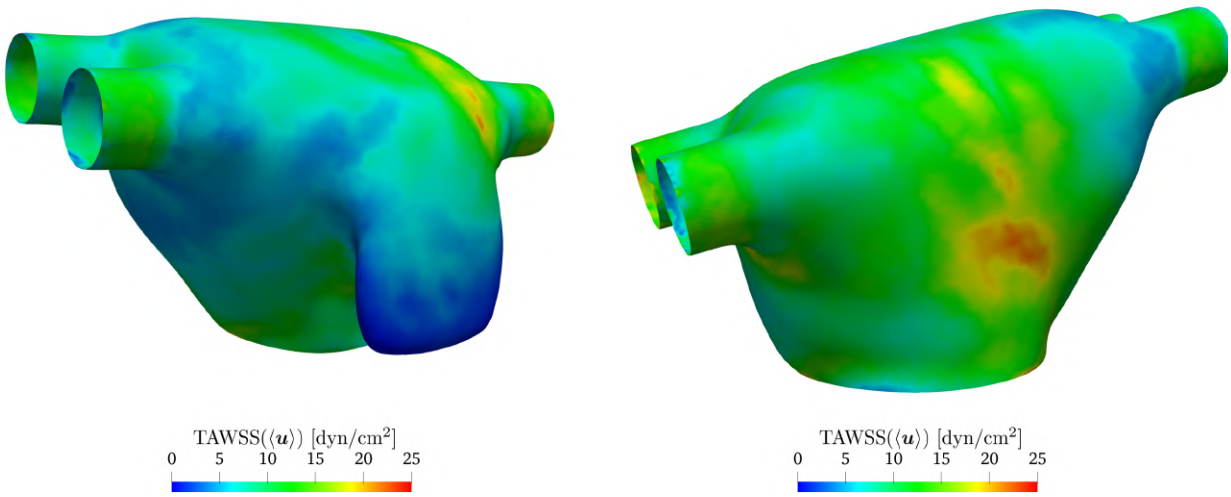

Figure 12: Reference solution: different views of time averaged wall shear stress (TAWSS).

ciated in the opposite side of the chamber, in accordance with the large values of $|\mathbf{WSS}|$ previously observed due to the interaction among the vortices and the endocardium.

In Figure 13 we report the OSI computed in the same settings of Figure 12. The OSI is large on the top of the LA where a large recirculation is present and on the bottom of the LAA, revealing hence a significant variation of the wall shear stress.

As a qualitative indication of the time that a fluid particle spends in the vicinity of the wall, we report in Figure 14 the RRT: as expected, the largest values are attained in the bottom of the LAA. We suggest it could be related to the shape and position of the LAA, where the blood reaches very low velocities and recirculation effects are observed. Interestingly, analogous considerations in terms of all the analysed hemodynamic indicators are found in healthy patient-specific studies as highlighted in [16], both in terms of magnitude and their distribution on the LA surface.

Large values of RRT in the LAA suggest the stasis of blood particles, i.e. the coagulation of blood in low velocity regions, which may result in the formation of blood clots [40, 62]. For this reason, we want to count the number of blood particles remaining in the LA at the end of each heart-cycle. Thus, we inject in the chamber a number particles $n(t)$ that is proportional to the inlet flux $Q_{\text{in}}(t) = \sum_{i=1}^{4} Q_{\text{PV}_i}(t)$ as:

$$n(t) = N_p \frac{Q_{\text{in}}(t)}{\max\limits_{t \in [0, T_{\text{HB}}]} Q_{\text{in}}(t)}, \tag{44}$$

being N_p the maximum number particles injected at a specific time. In particular, we populate the LA with $n(t)$ particles only during the first heartbeat, and, at the end of each heart-cycle, we count how many particles are left inside the LA. As shown in Figure 15a, particles injection in the PVs is achieved by considering four squares of edge $2R$ (inlet sections diameter) discretized with a cartesian grid with element size $\delta(t)$. In a single PV,

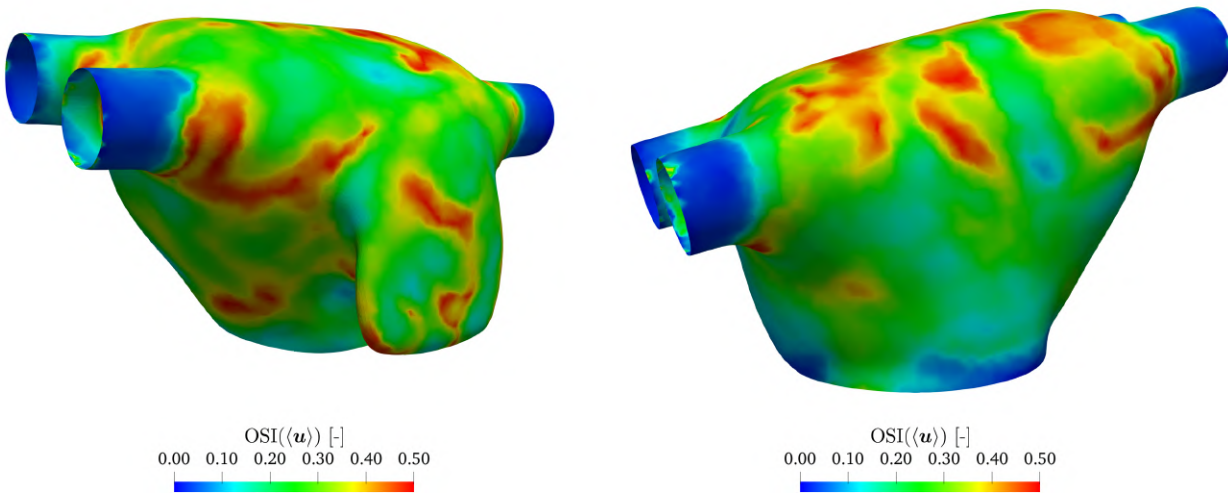

Figure 13: Reference solution: different views of oscillatory shear index (OSI)

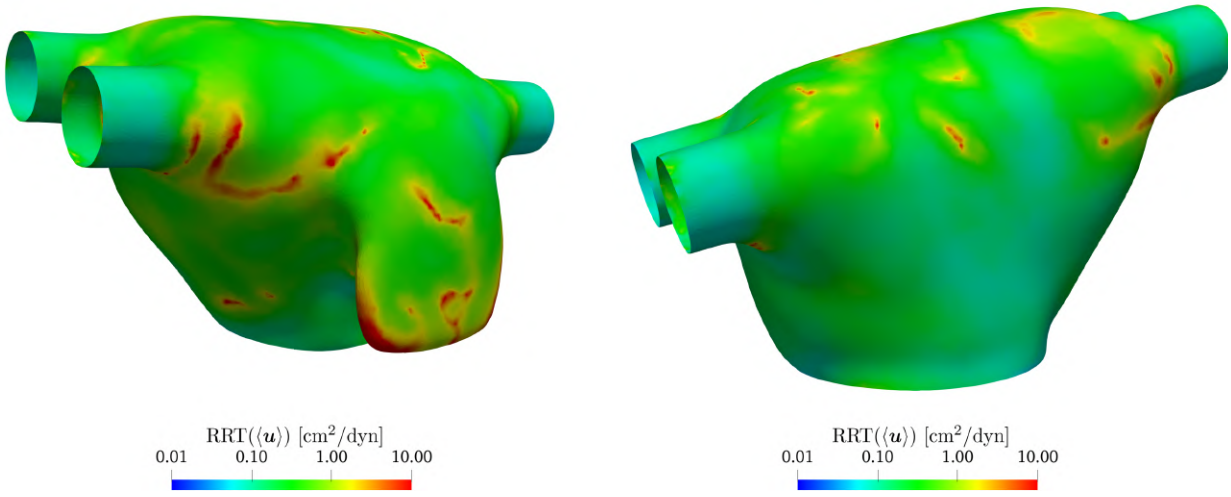

Figure 14: Reference solution: different views of relative residence time (RRT).

at time t, the number of particles entering in the LA is $\frac{n(t)}{4}$, which can be approximated as

$$\frac{n(t)}{4} \approx \left(\frac{2R}{\delta(t)} - 1 \right)^2 . \tag{45}$$

Using Eq. (44), the following expression of time-varying grid element size holds:

$$\delta(t) = R \left(\sqrt{N_p \frac{Q_{\text{in}}(t)}{\max\limits_{t \in [0, T_{\text{HB}}]} Q_{\text{in}}(t)}} + 2 \right)^{-1} , \tag{46}$$

which suggests that high flow rates correspond to small grid elements and therefore more particles are introduced. In Figure 15b, we report the behaviour of the grid element size in

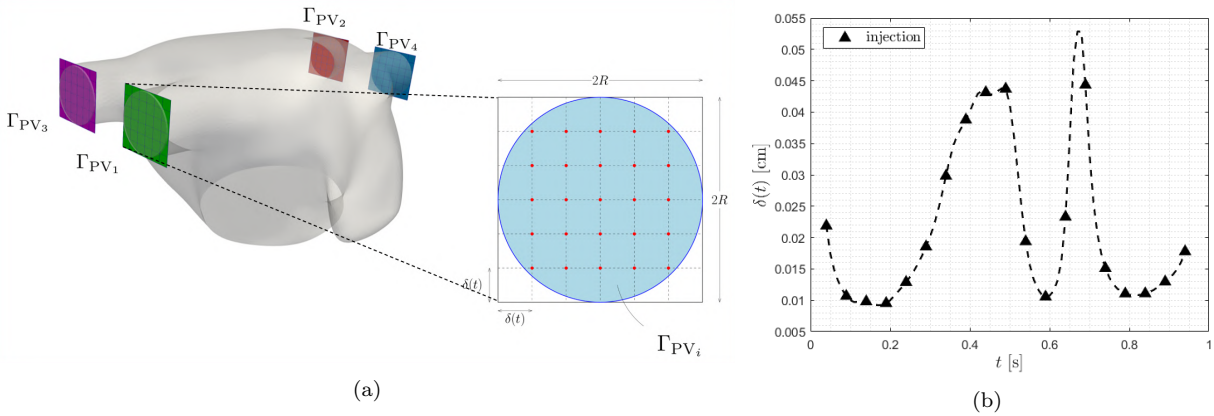

(a) (b)

Figure 15: Details on the methodology adopted to estimate number of particles. Four grids built around the PVs of the LA with a focus on the grid (in red the $n(t)/4$ particles entering in each vein) (left). The behaviour of the grid element size $\delta(t)$ in time, with triangles, we denote the particles injection instants (every 0.05 s) (right).

time. In particular, we inject particles in the four PVs every 0.05 s, obtaining, as expected, a profile proportional to the inlet flux, as reported in Figure 17a. In Figure 16 we report snapshots of the blood particles during six heartbeats, injecting in the first heart cycle only and leaving particles in the chamber for the following five cycles. We studied the contribution of particles coming from different veins representing with different colours particles from different inlets. We can observe the formation of four vortex rings coming from the PVs, with four jets impacting in the middle of the chamber and producing hence a mixing of particles. Particles remain inside the LAA, as also confirmed by large values of RRT previously found. In order to quantify wash-out effects, we stop particles introduction at $t = 1.00$ s, counting the number of particles at the end of each cycle. This result is then visualized in Figure 17b and quantified in Table 2. The overall number of particles introduced in the chamber during the first heartbeat is 50'471 and, at the end of each cardiac cycle, we report the percentage of particles still inside, showing that, after 5 cycles, in the LA there are the 0.08% of the total injected particles.

time [s]	$t = 1.00$	$t = 2.00$	$t = 3.00$	$t = 4.00$	$t = 5.00$	$t = 6.00$
particles	37'971	7'336	1'583	344	91	42
% on total injected	75.23	14.53	3.14	0.68	0.18	0.08

Table 2: Reference solution: particles remaining in the LA at the end of each cardiac cycle and percentage of particles on total injected.

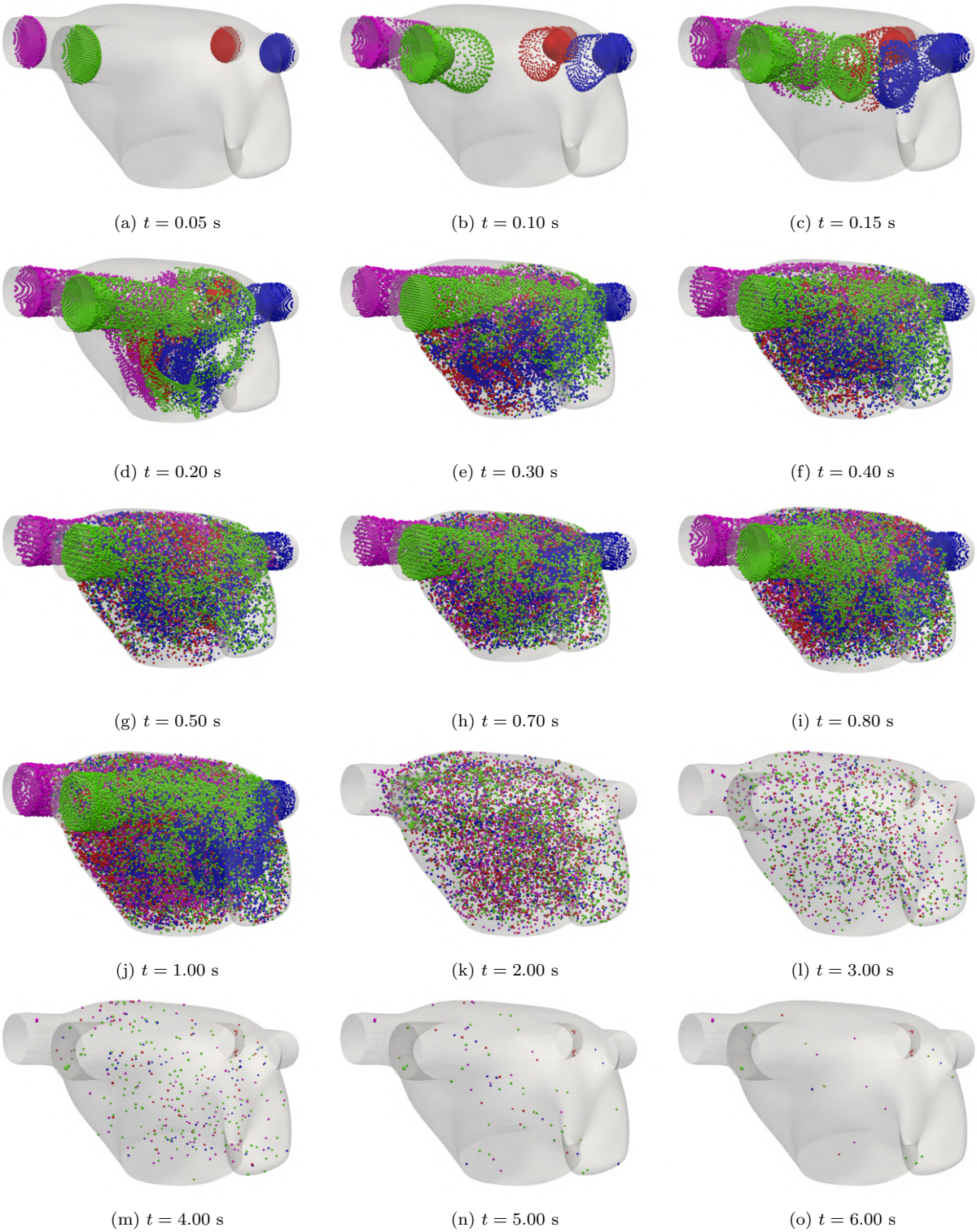

(a) $t = 0.05$ s (b) $t = 0.10$ s (c) $t = 0.15$ s

(d) $t = 0.20$ s (e) $t = 0.30$ s (f) $t = 0.40$ s

(g) $t = 0.50$ s (h) $t = 0.70$ s (i) $t = 0.80$ s

(j) $t = 1.00$ s (k) $t = 2.00$ s (l) $t = 3.00$ s

(m) $t = 4.00$ s (n) $t = 5.00$ s (o) $t = 6.00$ s

Figure 16: Reference solution: blood particles in the LA during six heartbeats, injecting particles for the first heartbeat only in a number proportional to the inlet flow rate. From (a) to (j) injection during the first cycle, from (k) to (o) particles remained inside the chamber at the end of each heart-cycle.

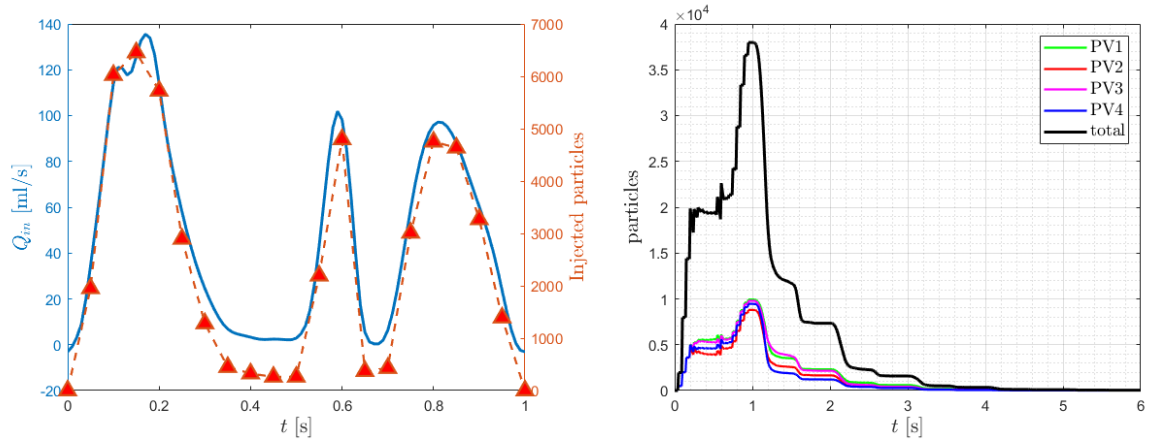

(a) (b)

Figure 17: Reference solution. Particles injected every 0.05 s (in red) are proportional to the inlet flow rate (in blue) (left). Number of particles inside the LA during 6 cardiac cycles, introducing particles in the first cycle only. With different colours: the number of particles in the chamber coming from different PVs (right).

4.2. Mesh convergence and comparison of SUPG and VMS-LES methods

We present a comparison between VMS-LES and SUPG stabilization techniques using the meshes $\mathcal{T}_{h_1}$ and $\mathcal{T}_{h_2}$. The results are compared with the reference solution of Section 4.1, which we remark has being obtained performing numerical simulation on the mesh $\mathcal{T}_{h_3}$ with SUPG stabilization technique. In Table 3, we summarize details of the five numerical simulations performed. Further features on the meshes adopted are given in Table 1.

Simulation ID	Mesh level	Δt [s]	Stabilization method
Reference	$\mathcal{T}_{h_3}$	$6.25 \cdot 10^{-5}$	SUPG
(a)	$\mathcal{T}_{h_2}$	$2.50 \cdot 10^{-4}$	SUPG
(b)	$\mathcal{T}_{h_2}$	$2.50 \cdot 10^{-4}$	VMS-LES
(c)	$\mathcal{T}_{h_1}$	$1.00 \cdot 10^{-3}$	SUPG
(d)	$\mathcal{T}_{h_1}$	$1.00 \cdot 10^{-3}$	VMS-LES

Table 3: Details on the numerical simulations used to compare SUPG and VMS-LES stabilization techniques in transitional regime. In all the simulations, we adopt $\mathbb{P}1 - \mathbb{P}1$ FE spaces, Backward Euler Method as time discretization scheme, and a semi-implicit treatment of the non linear terms.

We define some turbulent indicators obtained integrating suitable variables over the whole domain that are then compared with reference data in order to validate the results of the numerical simulations. Specifically, we compute the total kinetic energy of the flow, by using the phase-averaged velocity (defined in Eq. (36)), as

$$E_k\left(\langle \boldsymbol{u} \rangle\right) = \frac{1}{2}\rho \int_{\Omega_t} |\langle \boldsymbol{u} \rangle|_2^2 d\Omega. \tag{47}$$

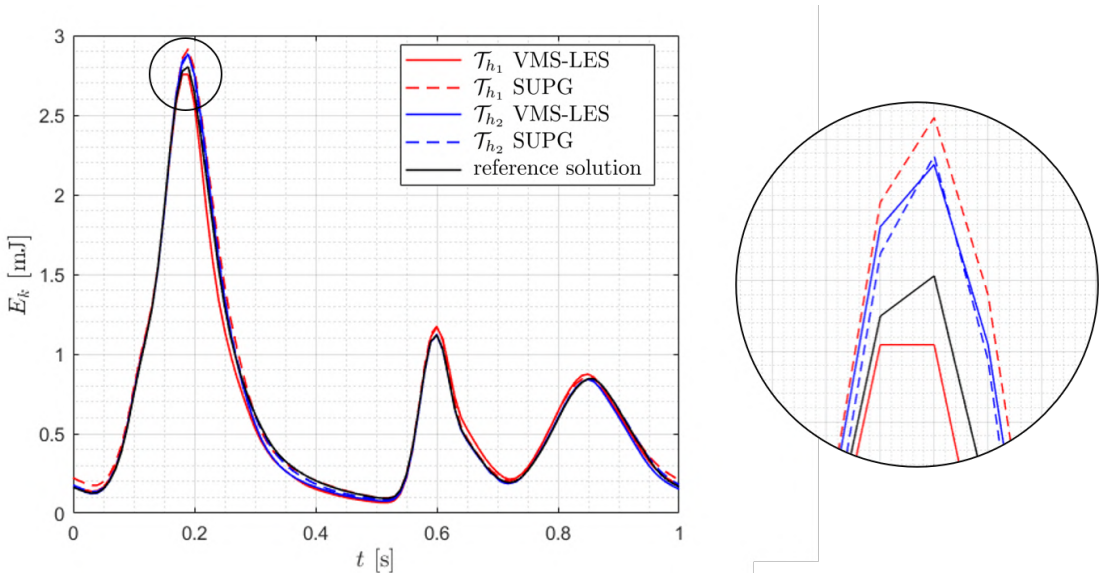

Figure 18: Total kinetic energy $E_k(\langle \boldsymbol{u} \rangle)$ using SUPG and VMS-LES models on meshes $\mathcal{T}_{h_1}$ and $\mathcal{T}_{h_2}$ compared to the reference solution; zoom on the first peak.

Moreover, we define the enstrophy of the flow as [34, 35]

$$S\left(\langle \boldsymbol{u} \rangle\right) = \frac{1}{2}\rho \int_{\Omega_t} |\nabla \times \langle \boldsymbol{u} \rangle|_2^2 d\Omega. \tag{48}$$

The latter is a fluid dynamics indicator that can be used to identify a transitional flow [34, 35]. Finally, we define the total fluctuating kinetic energy of the flow as [5, 30]

$$E_{kf}\left(\boldsymbol{\sigma_u}\right) = \frac{1}{2}\rho \int_{\Omega_t} |\boldsymbol{\sigma_u}|_2^2 d\Omega, \tag{49}$$

being $\boldsymbol{\sigma_u} = (\sigma_{u_1}, \sigma_{u_2}, \sigma_{u_3})^T$ a vector containing the standard deviation (i.e. the fluctuations) of each component k of the velocity field with respect to the phase-averaged velocity. Its k–th component is defined as

$$\sigma_{u_k}(\boldsymbol{x}, t) = \sqrt{\mathrm{var}(u_k(\boldsymbol{x}, t))} = \sqrt{\langle {u_k}^2(\boldsymbol{x}, t)\rangle - \langle u_k(\boldsymbol{x}, t)\rangle^2}, \quad k = 1, 2, 3. \tag{50}$$

The fluctuating kinetic energy is an important indicator of transition to turbulence but also provides informations on cycle-to-cycle variations. It can be seen as one of the most characteristic indicator of transitional flow for hemodynamic applications [5, 30].

In Figure 18, we report E_k computed on the reference solution and for the meshes $\mathcal{T}_{h_1}$ and $\mathcal{T}_{h_2}$ with SUPG and VMS-LES models. The total kinetic energy presents three peaks in correspondence of E-wave, A-wave and systolic filling phase. Energy production is observed when high-speed blood flows arrive from the PVs. As the jets impact in the middle of the cardiac chamber, dissipation of the kinetic energy can be appreciated. All the models and meshes share the same overall behaviour and coherent with the reference solution result.

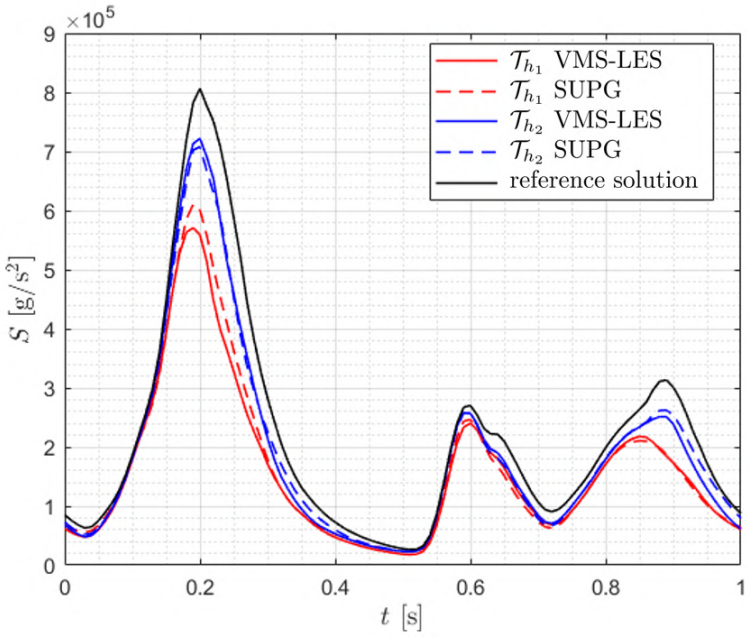

Figure 19: Enstrophy $S(\langle \boldsymbol{u} \rangle)$ using SUPG and VMS-LES models on meshes $\mathcal{T}_{h_1}$ and $\mathcal{T}_{h_2}$ compared to the reference solution.

For the mesh $\mathcal{T}_{h_2}$, the results are almost always comparable, whereas small differences can be appreciated in correspondence of the first peak among VMS-LES and SUPG on the mesh $\mathcal{T}_{h_1}$: with a coarse level, we see how the VMS-LES model seems to represent more accurately our reference solution, whereas SUPG overestimates it.

In Figure 19, we show the enstrophy S computed on the reference solution and for the meshes $\mathcal{T}_{h_1}$ and $\mathcal{T}_{h_2}$ with both SUPG and VMS-LES models. As for the total kinetic energy E_k, we observe three main peaks during the hearbeat in correspondence of the production and consequent dissipation of vorticity. The solution largely depends on the underlying mesh and, as it is refined, the solution becomes more accurate and no remarkable differences among the models can be appreciated.

Differently from the total kinetic energy and the enstrophy, we found more appreciable differences in the fluctuating kinetic energy E_{kf} as can be seen in Figure 20. We observe that the E_{kf} shows a peak with a large amplitude immediately after the E-wave. This result suggests that velocity fluctuations $\boldsymbol{\sigma_u}$ are higher during the first peak mainly due to small differences in the location of the shear layer and the vortical structures (where velocity gradients are high), as observed also in [5]. Moreover, we highlight this by reporting in Figure 21 the specific fluctuating kinetic energy ($\frac{1}{2}\rho|\boldsymbol{\sigma_u}|^2$) on a slice passing through the four PVs at time $t = 0.25$ s. It can be observed in fact that the largest values are obtained in the area where jets and vortical structures impact. Comparing the behaviour of E_{kf} adopting different mesh and models, we can observe that, on the one hand, the solutions obtained with SUPG and VMS-LES models on the mesh $\mathcal{T}_{h_2}$ are very similar and both are close to the reference solution, except from the third peak (zoom B) where the VMS-

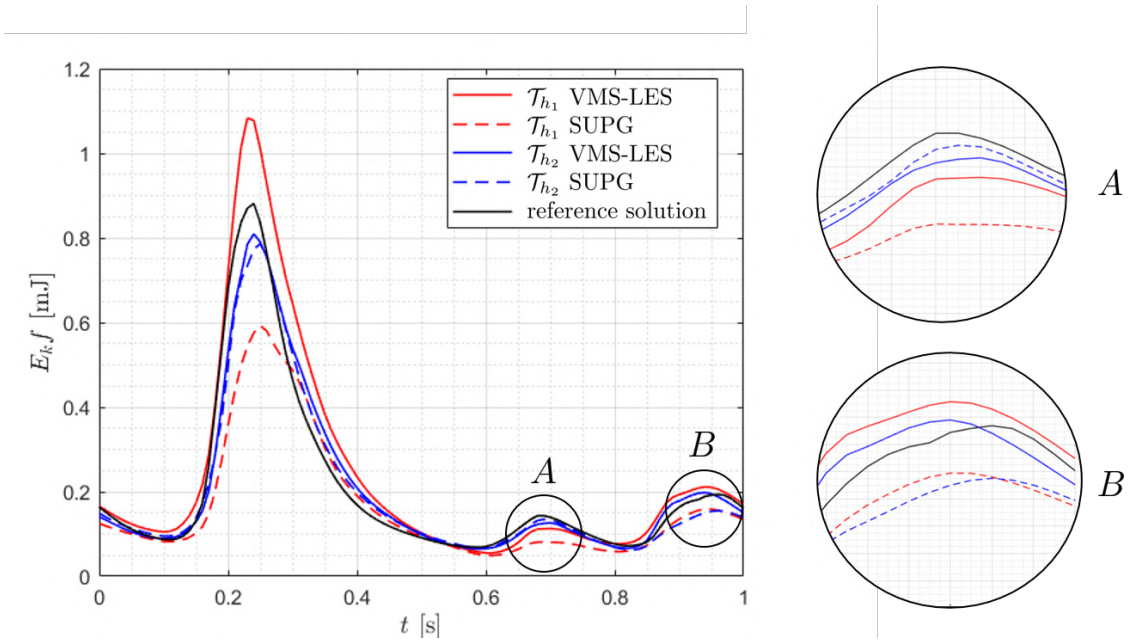

Figure 20: Fluctuating kinetic energy $E_{kf}(\boldsymbol{\sigma_u})$ using SUPG and VMS-LES models on meshes $\mathcal{T}_{h_1}$ and $\mathcal{T}_{h_2}$ compared to the reference solution; zooms on the second and third peak.

LES model better predicts the result obtained with the reference grid. On the other hand, remarkable differences are observed for the coarse grid. As a matter of fact, the amplitude of the first peak is highly dependent on the stabilization technique: they are both inaccurate with respect to the reference solution, but the coarse VMS-LES solution produces a lower relative error than the coarse SUPG (21.59% vs. 32.95%). Moreover, the VMS-LES solution on $\mathcal{T}_{h_1}$ is more accurate than the SUPG solution on the same mesh in the whole heartbeat (as confirmed also by zoom A and zoom B). Thus, we can see that, in terms of E_{kf}: (1) as expected, the effect of the turbulence model starts to vanish as the mesh becomes finer (since comparable results with SUPG and VMS-LES adopting the mesh $\mathcal{T}_{h_2}$ are achieved); (2) with relatively coarse meshes, VMS-LES better captures the fluctuating kinetic energy, being the latter an accurate indicator of transition to turbulence and of cycle-to-cycle flow variations, two relevant properties of cardiovascular flows.

5. Conclusions

In this paper, we simulated the hemodynamics of an idealized human LA with the goal of better characterizing and understanding the blood flow behavior in this little explored chamber. We used the standard SUPG and the VMS-LES stabilization methods to yield stable, discrete formulations of the Navier-Stokes equations approximated by means of the Finite Element method and to take into account of turbulence modelling (in the case of VMS-LES). The ALE formulation with prescribed deformation of the computational domain has been considered in combination with the Navier-Stokes solver. We run simulations on a fine mesh for six heartbeats discarding the first two in order to forget the influence of the

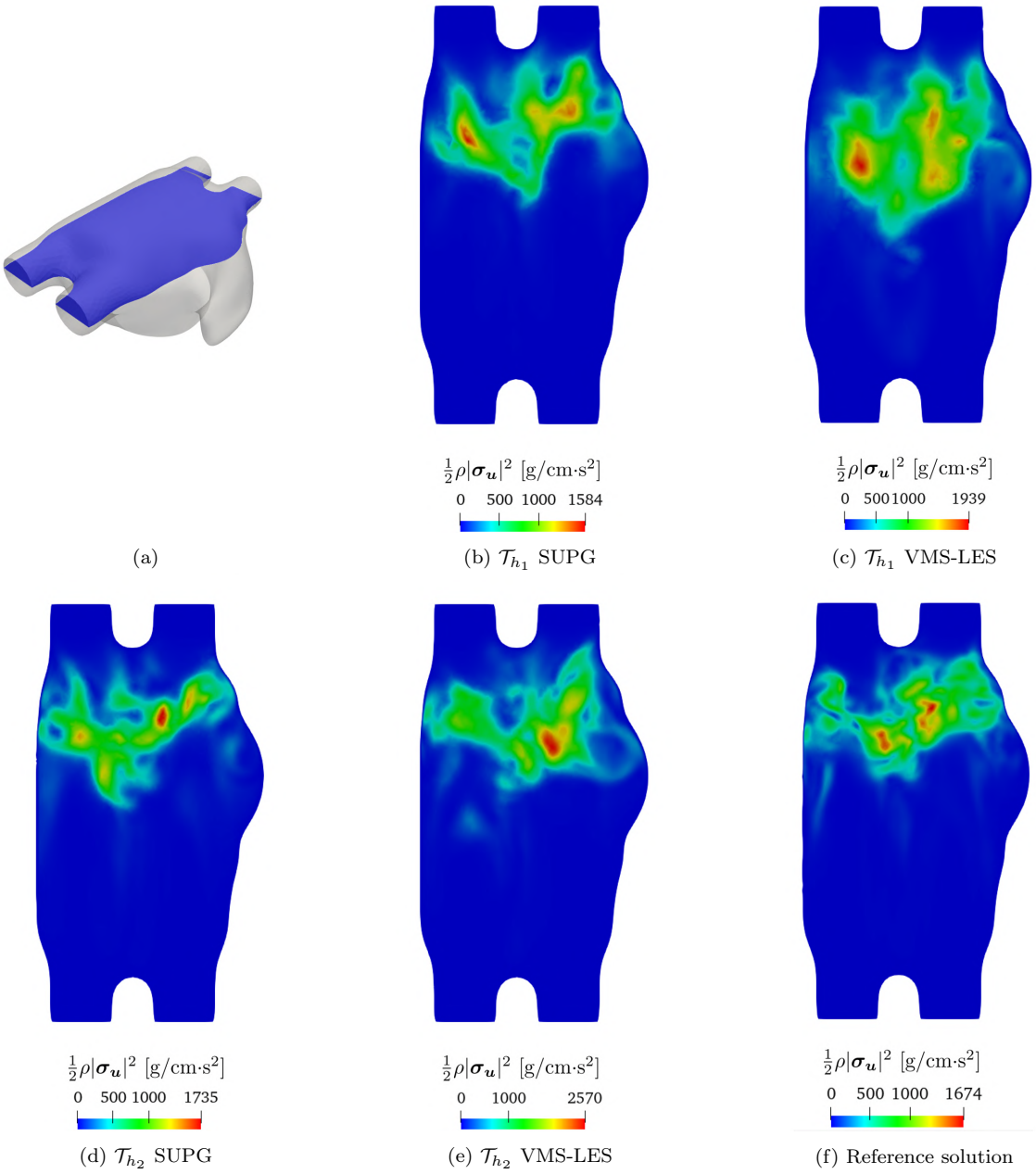

(a) (b) $\mathcal{T}_{h_1}$ SUPG (c) $\mathcal{T}_{h_1}$ VMS-LES

(d) $\mathcal{T}_{h_2}$ SUPG (e) $\mathcal{T}_{h_2}$ VMS-LES (f) Reference solution

Figure 21: Specific fluctuating kinetic energy $\frac{1}{2}\rho|\boldsymbol{\sigma_u}|$ on a slice passing through the four PVs (see (a)) at time $t = 0.25$ s using different meshes and models. Large values of fluctuating velocities are observed in the region of impact among jets.

initial conditions. The result obtained plays the role of our reference solution and it shows some characteristic blood flow features in the LA. The formation of vortex rings from the PVs is the main process occurring in this chamber. The impact of flow jets from the PVs and vortices breakup induce blood mixing and large values of the WSS in the wall nearby the impact regions. Large variability among the cardiac cycles is observed too. This, in

combination with other fluid dynamics indicators, highlights that the blood flow in the LA (in these idealized physiological conditions) is definitely neither laminar nor fully turbulent, but rather transitional. Such transitional nature of the blood flow is also highlighted in the LV cavity as shown e.g. in [5, 31]. A further indication that we deduce from our study is that the blood velocity profile at the MV section considerably departs from that of a flat or a Poiseuille profile, an assumption that is often, but incorrectly made when simulating LV hemodynamics; this result is coherent with the findings of [30, 31]. As a matter of fact, we found that the formation of vortices above the MV section produces low velocities and recirculation regions. We computed hemodynamic indicators and we deduced that a significant variation of WSS is observed in the bottom of the LAA and on the top of the LA. In particular, in the LAA low velocities and recirculation effects are observed, with consequent high values of RRT which suggests blood stasis. To quantify the latter, we propose a method useful to compute the number of particles inside a chamber. Finally, we present a mesh refinement study combined with an analysis on the numerical results obtained by means of the SUPG and VMS-LES stabilization techniques. We compute total kinetic energy and enstrophy based on the velocity field phase-averaged on four heartbeats, and we compare these results with our reference solution. In terms of these turbulence indicators, we found that, as the mesh is refined, the solution is more accurate using both stabilization techniques. In particular, discrepancies among models become less evident as the mesh become finer. Furthermore, we compared our results in terms of fluctuating kinetic energy, based on the standard deviation of the velocity field. This is an important measure in hemodynamic applications since it represents an indicator of cycle-to-cycle variations and also of transitional flow regimes. We found that the position where jets and vortices impact is highly variable from cycle-to-cycle, producing hence high values of fluctuating kinetic energy. In particular, we found that VMS-LES is able to better capture such variations in the flow, being always more accurate than the standard SUPG stabilization method. These differences are more evident using a coarse mesh, proving that VMS-LES model for relatively coarse meshes is more accurate to capture transitional effects in hemodynamics applications than the standard SUPG model.

Acknowledgments

This work has been supported by the ERC Advanced Grant iHEART, "An Integrated Heart Model for the simulation of the cardiac function", 2017–2022, P.I. A. Quarteroni (ERC–2016– ADG, project ID: 740132). We gratefully acknowledge the CINECA award under the ISCRA C initiative, for the availability of high performance computing resources and support under the project Computational Fluid Dynamics of Human Heart (CFDHH, P.I. A. Zingaro, 2020-2021). Finally, the authors acknowledge Dr. Davide Forti for fruitful discussions about this topic.

References

[1] D. Mozaffarian, E.J. Benjamin, et al., *Heart disease and stroke statistics-2015 update: a report from the American Heart Association*, Circulation, 2015.

[2] W.Y. Kim, P.G. Walker, E.M. Pedersen, J.K. Poulsen, S. Oyre, K. Houlind, and A.P. Yoganathan, *Left ventricular blood flow patterns in normal subjects: a quantitative analysis by three-dimensional magnetic resonance velocity mapping*, Journal of the American College of Cardiology, Vol. 26, pp. 224-238, 1995.

[3] M. Kanski, P. Arvidsson, J. Töger, R. Borgquist, E. Heiberg, M. Carlsson, H. Arheden, *Left ventricular fluid kinetic energy time curves in heart failure from cardiovascular magnetic resonance 4D flow data*, Journal of Cardiovascular Magnetic Resonance, 17:111, 2015.

[4] S.Z. Zhao, P. Papathanasopoulou, Q. Long, I. Marshall, X.Y. Xu, *Comparative study of magnetic resonance imaging and image-based computational fluid dynamics for quantification of pulsatile flow in a carotid bifurcation phantom*, Annals of Biomedical Engineering, Vol. 31, pp. 962-971, 2003.

[5] C. Chafna, S. Mendez, F. Nicoud, *Image based large-eddy simulation in a realistic left heart*, Computers & Fluids, Vol. 94, pp. 173-187, 2014.

[6] A. Quarteroni, L. Dede', A. Manzoni and C. Vergara, *Mathematical Modelling of the Human Cardiovascular System. Data, Numerical Approximation, Clinical Applications*, Cambridge University Press, 2019.

[7] A. Quarteroni, T. Lassila, S. Rossi and R. Ruiz-Baier, *Integrated Heart - Coupling multiscale and multiphysics models for the simulation of the cardiac function*, Computer Methods in Applied Mechanics and Engineering, Vol. 314, pp. 345-407, 2017.

[8] J.O. Mangual, E. Kraigher-Krainer, A. De Luca, L. Toncelli, A. Shah, S. Solomon, G. Galanti, F. Domenichini, and G. Pedrizzetti *Comparative numerical study on left ventricular fluid dynamics after dilated cardiomyopathy*, Journal of Biomechanics, Vol. 46, pp. 1611-1617, 2013.

[9] H. Watanabe, S. Sugiura, H. Kafuku, and T. Hisada, *Multiphysics simulation of left ventricular filling dynamics using fluid-structure interaction finite element method*, Biophysical Journal, Vol. 87, pp. 2074-2085, 2004.

[10] M. Nobili, U. Morbiducci, R. Ponzini, C.D. Gaudio, A. Balducci, M. Grigioni, F.M. Montevecchi, A. Redaelli, *Numerical simulation of the dynamics of a bileaflet prosthetic heart valve using a fluid-structure interaction approach*, Journal of Biomechanics, Vol. 41, pp. 2539-2550, 2008.

[11] T. Korakianitis, Y. Shi, *Numerical simulation of cardiovascular dynamics with healthy and diseased heart valves*, Journal of Biomechanics, Vol. 39, pp. 1964-1982, 2006.

[12] P. Tricerri, L. Dedè, A. Gambaruto, A. Quarteroni, A. Sequeira, *A numerical study of isotropic and anisotropic constitutive models with relevance to healthy and unhealthy cerebral arterial tissues*, International Journal of Engineering Science, Vol. 101, pp. 126-155, 2016.

[13] S.M. Szilágyi, L. Szilágyi, Z. Benyó, *A patient specific electro-mechanical model of the heart*, Computer Methods and Programs in Biomedicine, Vol. 101 (2), pp. 183-200, 2011.

[14] P. Colli Franzone, L.F. Pavarino and S. Scacchi, *Parallel multilevel solvers for the cardiac electromechanical coupling*, Applied Numerical Mathematics, Vol. 95, pp.140-153, 2015.

[15] V. Vedula, R. George, L. Younes and R. Mittal, *Hemodynamics in the left atrium and its effect on ventricular flow patterns*, Journal of Biomechanical Engineering, Vol. 137 (11), 111003, 2015.

[16] R. Koizumi, K. Funamoto, T. Hayase, Y. Kanke, M. Shibata, Y. Shiraishi, T. Yambe, *Numerical analysis of hemodynamic changes in the left atrium due to atrial fibrillation*, Journal of Biomechanics, Vol. 48, pp. 472-478, 2015.

[17] C.M. Colciago, S. Deparis and A. Quarteroni, *Comparisons between reduced order models and full 3D models for fluid-structure interaction problems in hemodynamics*, Journal of Computational and Applied Mathematics, Vol. 265, pp. 120-138, 2014.

[18] D.C. Wilcox, *Turbulence Modeling for CFD*, DCW Industries, Inc., 2006.

[19] F.R. Menter, M. Kuntz, R. Langtry, *Ten years of industrial experience with the SST turbulence model*, Turbulence, heat and mass transfer, Begell House Inc., pp. 625-632, 2003.

[20] M. Germano, U. Piomelli, P. Moin, W.H. Cabot, *A dynamic subgrid-scale eddy viscosity model*, Physics of Fluids, Vol. 3 (7), 1991.
[21] S.B. Pope, *Turbulent flows*, Cambridge University Press, 2000.
[22] Y. Bazilevs, V.M. Calo, J.A. Cottrell, T.J.R. Hughes, A. Reali, G. Scovazzi, *Variational multiscale residual-based turbulence modeling for Large Eddy Simulation of incompressible flows*, Computer Methods in Applied Mechanics and Engineering, Vol. 197, pp. 173-201, 2007.
[23] D. Forti, L. Dedè, *Semi-implicit BDF time discretization of the Navier-Stokes equations with VMS-LES modeling in a High Performance Computing framework*, Computers & Fluids, Vol. 117, pp. 168-182, 2015.
[24] Y. Bazilevs, K. Takizawa, T.E. Tezduyar, M.-C. Hsu, N. Kostov, S. McIntyre, *Aerodynamic and FSI Analysis of Wind Turbines with the ALE-VMS and ST-VMS Methods*, Archives of Computational Methods in Engineering, Vol. 21 (4), pp. 359-398, 2014.
[25] J. Donea, S. Giuliani, and J.P. Halleux, *An arbitrary Lagrangian-Eulerian finite element method for transient dynamic fluid-structure interactions*, Computer Methods in Applied Mechanics and Engineering, Vol. 33, pp. 689-723, 1982.
[26] A.A. Johnson and T.E. Tezduyar, *Mesh update strategies in parallel finite element computations of flow problems with moving boundaries and interfaces*, Computer Methods in Applied Mechanics and Engineering, Vol. 119, pp. 73-94, 1994.
[27] A.S. Patelli, L. Dedè, T. Lassila, A. Bartezzaghi, A. Quarteroni, *Isogeometric approximation of cardiac electrophysiology models on surfaces: an accuracy study with application to the human left atrium*, Computer Methods in Applied Mechanics and Engineering, Vol. 317, pp. 248-273, 2017.
[28] *LifeV*. Repository of the library available at `https://bitbucket.org/lifev-dev/lifev-release/wiki/Home`. Last access 22 October 2020.
[29] A. Masci, M. Alessandrini, D. Forti, F. Menghini, L. Dedè, C. Tommasi, A. Quarteroni, C. Corsi, *A Patient-Specific Computational Fluid Dynamics Model of the Left Atrium in Atrial Fibrillation: Development and Initial Evaluation*, proceedings of the Functional Imaging and Modelling of the Heart conference, FIMH 2017, LNCS 10263, pp. 392-400, 2017.
[30] A. Tagliabue, L. Dedè, A. Quarteroni, *Fluid dynamics of an idealized left ventricle: the extended Nitsche's method for the treatment of heart valves as mixed time varying boundary conditions*, International Journal for Numerical Methods in Fluids, Vol. 85 (3), pp. 135-164, 2017.
[31] A. Tagliabue, L. Dedè, A. Quarteroni, *Complex blood flow patterns in an idealized left ventricle: a numerical study*, Chaos, Vol. 27 (9), pp. 093939, 2017.
[32] D.N. Ku, D.P. Giddens, C.K. Zarins, S. Glagov, *Pulsatile flow and athero-sclerosis in the human carotid bifurcation. Positive correlation between plaque location and low oscillating shear stress*, Arteriosclerosis, Vol. 5, pp. 293-302, 1985.
[33] H.A Himburg, D.M. Grzybowski, A.L. Hazel, J.A. LaMack, X.M. Li, M.H. Friedman , *Spatial comparison between wall shear stress measures and porcine arterial endothelial permeability*, American Journal of Physiology: Heart and Circulatory Physiology, Vol. 286, pp. 1916-1922, 2004.
[34] M. Umeki, *Numerical simulation of plane Poiseuille turbulence*, Fluid Dynamics Research, Vol. 13, pp. 67-79, 1994.
[35] A.R. Lupo, I.I. Mokhov, S. Dostoglou, A.R. Kunz, J.P. Burkhardt, *Assessment of the Impact of the Planetary Scale on the Decay of Blocking and the Use of Phase Diagrams and Enstrophy as a Diagnostic*, Izvestiya, Atmospheric and Oceanic Physics, Vol. 43 (1), pp. 45-51, 2007.
[36] Y. Bazilevs, J.R. Gohean, T.J.R. Hughes, R.D. Moser, Y. Zhang, *Patient-specific isogeometric fluid-structure interaction analysis of thoracic aortic blood flow due to implantation of the Jarvik 2000 left ventricular assist device*, Computer Methods in Applied Mechanics and Engineering, Vol. 198 (45-46), pp. 3534-3550, 2009.
[37] L. Antiga, M. Piccinelli, L. Botti, B. Ene-Iordache, A. Remuzzi, D.A. Steinman, *An image-based modeling framework for patient-specific computational hemodynamics*, Medical & Biological Engineering & Computing, Vol. 46, pp. 1097-1112, 2008.
[38] *CoMMLab: Computational Multiscale Simulation Lab*. Repository of computational physiology avail-

able at `https://commlab.uv.es/repository/`. Last access: 18 May 2020.
[39] A. Ferrer, R. Sebastián, D. Sánchez-Quintana, J.F. Rodríguez, Godoy E.J., L. Martinez, J. Saiz, *Detailed Anatomical and Electrophysiological Models of Human Atria and Torso for the Simulation of Atrial Activation*, PLoS ONE, Vol. 10(11): 1-29, 2015.
[40] D.K. Gupta, A.M. Shah, R.P. Giugliano, C.T. Ruff, E.M. Antman, L.T. Grip, N. Deenadayalu, E. Hoffman, I. Patel, M. Shi, M. Mercuri, V. Mitrovic, E. Braunwald, S.D. Solomon, *Left atrial structure and function in atrial fibrillation: ENGAGE AF-TIMI 48*, European Heart Journal, Vol. 35(22), pp. 1457–1465, 2014.
[41] C. Wiggers, *Circulation in Health & Diseases*, Lea & Febiger, Philadelphia, 1915.
[42] J.R. Mitchell, J. Wang, *Expanding application of the Wiggers diagram to teach cardiovascular physiology*, Advances in Physiology Education, Vol. 38(2), 170-175, 2014.
[43] J.H Seo, V. Vedula, T. Abraham, A. Lardo, F. Dawoud, H. Luo, R. Mittal, *Effect of the MV on diastolic flow patterns*, Physics of Fluids, Vol. 26 (12), 2014.
[44] X. Zheng, J. Seo, V. Vedula, T. Abraham, R. Mittal, *Computational modeling and analysis of intracardiac flows in simple models of the left ventricle*, European Journal of Mechanics - B/Fluids, Vol. 35, pp. 31–39, 2012.
[45] K.H. Fraser, M.E. Taskin, B.P. Griffith, Z.J. Wu, *The use of computational fluid dynamics in the development of ventricular assist devices.* Medical Engineering and Physics. Vol. 33(3), pp. 263-80, 2011.
[46] J. Zhang, Z. Chen, B.P. Griffith, Z.J. Wu, *Computational characterization of flow and blood damage potential of the new maglev CH-VAD pump versus the HVAD and HeartMate II pumps*, The International Journal of Artificial Organs. Vol. 43(10), pp. 653-662, 2020.
[47] S.J. Kovacs, D.M. McQueen, S.Peskin, *Modelling cardiac fluid dynamics and diastolic function*, Philosophical Transactions of The Royal Society B Biological Sciences, Vol. 359, pp. 1299-1314, 2001.
[48] M.T. Ngo, C.I. Kim, J. Jung, G.H. Chung, D.H. Lee, H.S. Kwak, *Four-Dimensional Flow Magnetic Resonance Imaging for Assessment of Velocity Magnitudes and Flow Patterns in The Human Carotid Artery Bifurcation: Comparison with Computational Fluid Dynamics*, Diagnostics (Basel), Vol. 9(4), 2019.
[49] Z. Stankovic, B.D. Allen, J. Garcia, K.B. Jarvis, M. Markl, *4D flow imaging with MRI*, Cardiovascular Diagnosis & Therapy. Vol. 4(2), pp. 173-192 2014.
[50] T.J.R. Hughes. *Multiscale phenomena: Greens functions, the Dirichlet-to-Neumann formulation, subgrid scale models, bubbles, and the origins of stabilized methods.* Computer Methods in Applied Mechanics and Engineering, Vol. 127, pp. 387-401, 1995.
[51] T.J.R. Hughes, V.M. Calo, G. Scovazzi *Variational and multiscale methods in turbulence.* In: W. Gutkowski, T.A. Kowalewski, editors. Mechanics of the 21st century. Amsterdam: Springer. pp. 153–63, 2005.
[52] T.J.R. Hughes, L. Mazzei, K.E. Jansen *Large-eddy simulation and the variational multiscale method*, Computing and Visualization in Science, Vol. 3, pp. 47–59, 2000.
[53] T.J.R. Hughes, A.A. Oberai, L. Mazzei. *Large eddy simulation of turbulent channel flows by the variational multiscale method.* Physics of Fluids. 13(6), pp. 1784–99, 2001.
[54] T.J.R. Hughes, G. Scovazzi, L.P. Franca. *Multiscale and stabilized methods.* In: E. Stein, R. de Borst, T.J.R. Hughes, editors. Encyclopedia of computational mechanics. John Wiley & Sons, 2004.
[55] A. Quarteroni *Numerical Models for Differential Problems*, MS&A, 16, Springer, 2017.
[56] T.J.R. Hughes, *The Finite Element Method. Linear Static and Dynamic Finite Element Analysis*, Courier Corporation, 1987.
[57] A. Quarteroni, F. Saleri, R. Sacco, *Numerical mathematics*, Springer, 2007.
[58] L. Bertagna, S. Deparis, L. Formaggia, D. Forti, A. Veneziani, *The LifeV library: engineering mathematics beyond the proof of concept*, arXiv preprint arXiv:1710.06596, 2017.
[59] J.C.R. Hunt, A.A. Wray, P. Moin, *Eddies, stream, and convergence zones in turbulent flows*, Center for Turbulence Research Report CTR-S88, pp. 193-208, 1988.
[60] M. Fedele. A. Quarteroni, *Polygonal surface processing and mesh generation tools for numerical sim-*

ulations of the complete cardiac function, MOX report, Politecnico di Milano, 32, 2019.

[61] M. Domanin, A. Buora, F. Scardulla, B. Guerciotti, L. Forzenigo, P. Biondetti, C. Vergara, *Computational Fluid-Dynamic Analysis after Carotid Endarterectomy: Patch Graft versus Direct Suture Closure*, Annals of Vascular Surgery, Vol. 44, pp. 325-335, 2017.

[62] D. Dillon-Murphy, D. Marlevi, B. Ruijsink, A. Qureshi, H. Chubb, E. Kerfoot, M. O'Neill, D. Nordsletten, O. Aslanidi, A. de Vecchi, *Modeling Left Atrial Flow, Energy, Blood Heating Distribution in Response to Catheter Ablation Therapy*, Frontiers in Physiology, Vol. 14, 2018.

[63] Meshes for LA fluid dynamics simulations. Available at `https://gitlab.com/albertozingaro/cfd-mesh`.

MOX Technical Reports, last issues

Dipartimento di Matematica
Politecnico di Milano, Via Bonardi 9 - 20133 Milano (Italy)

78/2020 Regazzoni, F.; Salvador, M.; Africa, P.c.; Fedele, M.; Dede', L.; Quarteroni, A.
A cardiac electromechanics model coupled with a lumped parameters model for closed-loop blood circulation. Part II: numerical approximation

79/2020 Regazzoni, F.; Salvador, M.; Africa, P.c.; Fedele, M.; Dede', L.; Quarteroni, A.
A cardiac electromechanics model coupled with a lumped parameters model for closed-loop blood circulation. Part I: model derivation

77/2020 Parolini, N.; Ardenghi, G.;Dede’, L.; Quarteroni, A.
A Mathematical Dashboard for the Analysis of Italian COVID-19 Epidemic Data

76/2020 Centofanti, F.; Lepore, A.; Menafoglio, A.; Palumbo, B.; Vantini, S.
Functional Regression Control Chart

75/2020 F. Dassi; A. Fumagalli; D. Losapio; S. Scialò; A. Scotti; G. Vacca
The mixed virtual element method for grids with curved interfaces

74/2020 Formaggia, L; Fumagalli, A.; Scotti, A.
A multi-layer reactive transport model for fractured porous media

72/2020 Belli E.; Vantini S.
Measure Inducing Classification and Regression Trees for Functional Data

71/2020 Belli E; Vantini S.
Ridge regression with adaptive additive rectangles and other piecewise functional templates

70/2020 Belli E.
Smoothly Adaptively Centered Ridge Estimator

69/2020 Galvani, M.; Torti, A.; Menafoglio, A.; Vantini S.
FunCC: a new bi-clustering algorithm for functional data with misalignment